

¹ Identification of low energy nuclear recoils in a gas
² TPC with optical readout

³ E Baracchini^{1,2}, L Benussi³, S Bianco³, C Capoccia³, M
⁴ Caponero^{3,4}, G Cavoto^{5,6}, A Cortez^{1,2}, I A. Costa⁷, E Di
⁵ Marco⁵, G D'Imperio⁵, G Dho^{1,2}, F Iacoangeli⁵, G Maccarrone³,
⁶ M Marafini^{5,8}, G Mazzitelli³, A Messina^{5,6}, R A. Nobrega⁷, A
⁷ Orlandi³, E Paoletti³, L Passamonti³, F Petrucci^{9,5}, D Piccolo³,
⁸ D Pierluigi³, D Pinci⁵, F Renga⁵, F Rosatelli³, A Russo³, G
⁹ Saviano^{3,10} R Tesauro³, and S Tomassini³

¹⁰ Gran Sasso Science Institute, L'Aquila, Italy

¹¹ INFN, Laboratori Nazionali del Gran Sasso, Assergi, Italy

¹² INFN, Laboratori Nazionali di Frascati, Frascati, Italy

¹³ ENEA Centro Ricerche Frascati, Frascati, Italy

¹⁴ INFN, Sezione di Roma, Roma, Italy

¹⁵ Dipartimento di Fisica, Sapienza Università di Roma, Roma, Italy

¹⁶ Universidade Federal de Juiz de Fora, Juiz de Fora, Brasil

¹⁷ Museo Storico della Fisica e Centro Studi e Ricerche “Enrico Fermi”, Roma, Italy

¹⁸ Dipartimento di Matematica e Fisica, Università Roma TRE, Roma, Italy

¹⁹ ²⁰ Dipartimento di Ingegneria Chimica, Materiali e Ambiente, Sapienza Università di Roma, Roma, Italy

E-mail: emanuele.di.marco@roma1.infn.it

May 2020

Abstract. The search for a novel technology able to detect and reconstruct nuclear recoil events in the keV energy range has become more and more important as long as vast regions of high mass WIMP-like Dark Matter candidate have been excluded. Gaseous Time Projection Chambers (TPC) with optical readout are very promising candidate combining the complete event information provided by the TPC technique to the high sensitivity and granularity of last generation scientific light sensors. A TPC with an amplification at the anode obtained with Gas Electron Multipliers (GEM) was tested at the Laboratori Nazionali di Frascati. Photons and neutrons from radioactive sources were employed to induce recoiling nuclei and electrons with kinetic energy in the range [1–100] keV. A He-CF₄ (60/40) gas mixture was used at atmospheric pressure and the light produced during the multiplication in the GEM channels was acquired by a high position resolution and low noise scientific CMOS camera and a photomultiplier. A multi-stage pattern recognition algorithm based on an advanced clustering technique is presented here. A number of cluster shape observables are used to identify nuclear recoils induced by neutrons originated from a AmBe source against X-ray ⁵⁵Fe photo-electrons. An efficiency of 18% to detect nuclear recoils with an energy of about 6 keV is reached obtaining at the same time a 96% ⁵⁵Fe photo-electrons suppression. This makes this optically readout gas TPC a very promising candidate for future investigations of ultra-rare events as directional direct Dark Matter searches.

42 1. Introduction

43 The advent of a market of high position resolution and single photon light sensors can
 44 open new opportunity to investigate ultra-low rate phenomena as Dark Matter (DM)
 45 particle scattering on nuclei in a gaseous target.

46 The nature of DM is still one of the key issues to understand our Universe [1, 2].
 47 Different models predict the existence of neutral particles with a mass of few GeVs or
 48 higher that would fill our Galaxy [3–6]. They could interact with the nuclei present in
 49 ordinary matter producing highly ionizing nuclear recoils but with a kinetic energy as
 50 small as few keVs. Moreover, given the motion of the Sun in the Milky Way towards the
 51 Cygnus constellation, such nuclear recoils would exhibit in galactic coordinate a dipole
 52 angular distribution in a terrestrial detector [7]. In this paper the use of a scientific
 53 CMOS camera to capture the light emitted by Gas Electron Multipliers (GEMs) in a
 54 Time Projection Chamber (TPC) device is described. The GEMs are located in the
 55 TPC gas volume at the anode position and are used to amplify the ionization produced
 56 in the gas by the nuclear recoils and other particles. A secondary scintillation light is
 57 produced in the amplification of the avalanche process by the GEM. This light and its
 58 spatial distribution is reconstructed in the detector and characterized by means of a
 59 clustering algorithm.

60 Different type of particles will produce distinctive and diverse patterns of ionization
 61 charge, and therefore of light emitted by the GEMs, given the different way they deposit
 62 energy and interact with matter. Therefore, nuclear recoils can be efficiently identified
 63 and separated from different kinds of background down to a few keV kinetic energy. The
 64 study of the optical readout of a TPC has been recently conducted with several small
 65 size prototypes (NITEC [8], ORANGE [9, 10], LEMON [11–13]) with various particle
 66 sources, in the context of the CYGNO project [14, 15]. In the following, the study of
 67 nuclear recoils excited by neutrons from an AmBe source and electron recoils from a
 68 ^{55}Fe source in the gas volume of the LEMON prototype is presented.

69 2. Experimental layout

70 A 7 liter active sensitive volume TPC (named LEMON) was employed to detect the
 71 particle recoils. A sketch (not to scale) of the detector setup is shown in Fig. 1 (left),
 72 while an image of the detector in the experimental area is shown in Fig. 1 (right). The
 73 sensitive volume where the ionization electrons are drifting features a $200 \times 240 \text{ mm}^2$
 74 elliptical field cage with a 200 mm distance between the anode and the cathode. The
 75 anode side is instrumented with a $200 \times 240 \text{ mm}^2$ rectangular triple GEM structure.
 76 Standard LHCb-like GEMs ($70 \mu\text{m}$ diameter holes and $140 \mu\text{m}$ pitch) [16] were used
 77 with two 2 mm wide transfer gaps between them. The light emitted from the GEMs is
 78 detected with an ORCA-Flash 4.0 camera [17] through a $203 \times 254 \times 1 \text{ mm}^3$ transparent
 79 window and a bellow of adjustable length. This camera is positioned at a 52 cm distance
 80 from the outermost GEM layer and is based on a sCMOS sensor with high granularity

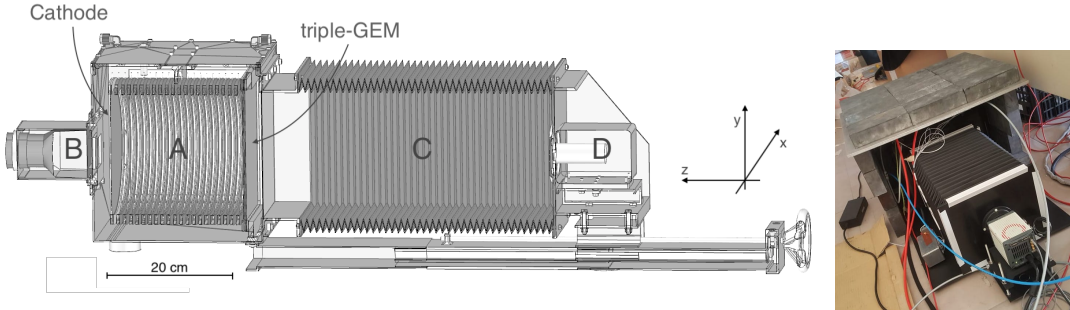


Figure 1. Left: the LEMON prototype with its 7 liter sensitive volume (A), the PMT (B), the adjustable bellow (C) and the sCMOS camera with its lens (D). Right: LEMON with the lead shield around the drift volume cage. The sCMOS camera (on the front) is looking at the GEMs through a blackened bellow.

(2048×2048 pixels), very low noise (around two photons per pixel), high sensitivity (70% quantum efficiency at 600 nm) and good linearity [18]. This camera is instrumented with a Schneider lens, characterized by an aperture $f/0.95$ and a focal length of 25 mm. The lens is placed at a distance $d = 50.6$ cm from the last GEM in order to obtain a de-magnification $\Delta = (d/f) - 1 = 19.25$ to image a surface $25.6 \times 25.6 \text{ cm}^2$ onto the $1.33 \times 1.33 \text{ cm}^2$ sensor. In this configuration, each pixel is therefore imaging an effective area of $125 \times 125 \mu\text{m}^2$ of the GEM layer. The fraction of the light collected by the lens is evaluated to be 1.7×10^{-4} [18]. A semi-transparent mesh was used as a cathode in order to collect light on that side also with a $50 \times 50 \text{ mm}^2$ HZC Photonics XP3392 photomultiplier [19] (PMT) detecting light through a transparent $50 \times 50 \times 4 \text{ mm}^3$ fused silica window. More details on the LEMON detector can be found in Ref. [20].

A 5 cm thick lead shielding was mounted around the LEMON field cage to reduce the environmental natural radioactivity background. From the measurements of the GEM current with and without the lead shielding, a factor two reduction in the total ionization within the sensitive volume, very likely due to environmental radioactivity, was estimated.

3. Particle images in the LEMON gas volume

The LEMON detector was operated in an overground location at Laboratori Nazionali di Frascati (LNF) with a He-CF₄ (60/40) gas mixture at atmospheric pressure, the triple GEM system set at a voltage across each GEM sides of 460 V and a transfer field between the GEM layers of 2.5 kV/cm. A six-independent-HV-channels CAEN A1257 module ensured stability and monitored the bias currents with a precision of 20 nA. The gas mixture was kept under continuous flow of about 200 cc/min and with the GEMs operated at a 2.0×10^6 electric gain. The typical photon yield for this type of gas mixtures has been measured to be around 0.07 photons per avalanche electron [18,21,22] and therefore the overall light gain is about 10^6 . The field cage was powered by a CAEN N1570 [23], generating an electric field of 0.5 kV/cm.

The motion of particles within the gas mixtures was studied by means of different simulation tools. In particular, GARFIELD [24, 25] program was used to evaluate the transport properties for ionization electrons in the sensitive volume for an electric field of 500 V/cm.

Given the diffusion in the gas, ionization electrons produced at a distance z from the GEM will distribute over a region on the GEM surface, having a Gaussian transverse profile with a σ given by:

$$\sigma = \sqrt{\sigma_0^2 + D^2 \cdot z}, \quad (1)$$

where D is the transverse diffusion coefficient, whose value at room temperature $140 \mu\text{m}/\sqrt{\text{cm}}$ was obtained with a simulation. The value of σ_0^2 was measured to be about $300 \mu\text{m}$ [26, 27]. Therefore, in average, a point-like ionization will result in a spot of [3–4] mm².

The expected effective ranges of electron and nuclear recoils were evaluated respectively with GEANT4 [28] and with SRIM [29] simulation programs. The recoil range estimated from simulation, as a function of the impinging particle kinetic energy, is shown in Fig. 2 for electrons and -as an example- for He-nuclei. These results show

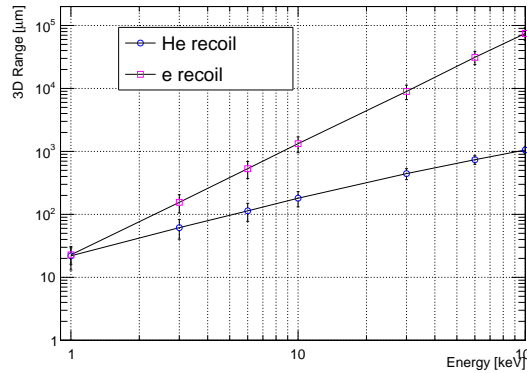


Figure 2. Average ranges for electron and He-nucleus recoils as a function of their initial kinetic energy.

that:

- He-nuclei recoils have a sub-millimeter range up to energies of 100 keV and are thus expected to produce bright spots with sizes mainly dominated by diffusion;
- low energy (less than 10 keV) electron recoils are in general longer than He-nucleus recoils with same energy and are expected to produce sparse and less intense spot-like signals. For a kinetic energy of 10 keV, the electron range becomes longer than 1 mm and for few tens of keV, tracks of few cm are expected.

The images collected by the sCMOS camera contain several instances of the particles tracks described above. The sCMOS sensor was operated in continuous mode with a global exposure time of 30 ms. Example images are shown in Fig. 3.

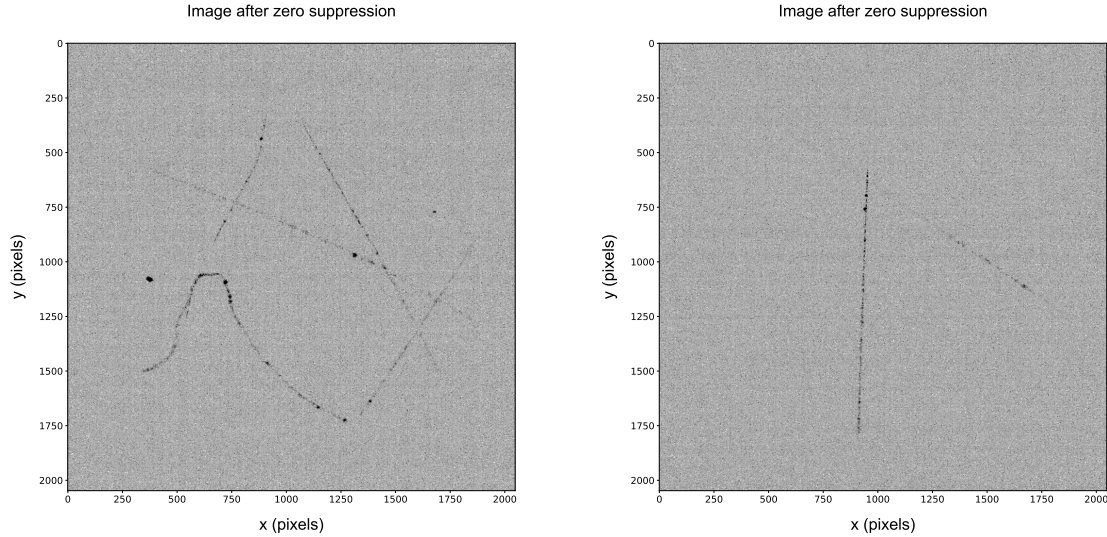


Figure 3. Two example pictures taken with the sCMOS camera with a 30 ms exposure time and with a common noise level subtracted (zero suppression), belonging to a data taking run without any artificial source. Left: cosmic tracks and natural radioactivity signals are present. Right: only two long cosmic rays tracks are visible. The coordinates are defined such that the vertical direction is along the y-axis and cosmic rays are expected to come from the top of the figure.

134 The PMT waveform was sent to a digitizer board with a sampling frequency of
 135 4 GS/s. The trigger scheme of the detector is based on the PMT signal: if, during the
 136 exposure time window, the PMT waveform exhibits a peak exceeding a threshold of
 137 80 mV, it is acquired in a time window of 25 μ s and the corresponding sCMOS image
 138 is stored. The digitizer is operated in single-event mode. No more than one 25 μ s long
 139 PMT waveform is recorded in each sCMOS exposure time, even if during the sCMOS
 140 exposure time several PMT signals are produced. Therefore, the PMT information was
 141 mainly exploited only to select events with a cosmic ray track.

142 Several light spots are visible with different ionization patterns due to different types
 143 of particles interacting in the gas. Figure 3 (left) shows an image with typical long tracks
 144 from cosmic rays traveling through the full gas volume, where clusters of light with larger
 145 energy deposition are clearly visible, superimposed to low energy electrons, very likely
 146 due to natural radioactivity. Figure 3 (right) shows an example of a cleaner event with
 147 two straight cosmic ray tracks, that can be used for energy calibration purposes, since
 148 the energy releases along the path, dE/dx , can be predicted given the gas mixture and
 149 pressure.

150 Two different artificial radioactive sources were employed for testing and studying
 151 the detector responses.

152 A **neutron** source, based on a 3.5×10^3 MBq activity ^{241}Am source contained in a
 153 Beryllium capsule (AmBe) was placed at a distance of 50 cm from the sensitive volume

154 side. Because of the interactions between α particles produced by the ^{241}Am and the
 155 Beryllium nuclei, the AmBe source isotropically emits:

- 156 • photons with an energy of 59 keV produced by ^{241}Am ;
- 157 • neutrons with a kinetic energy mainly in a range [1–10] MeV
- 158 • photons with an energy of 4.4 MeV produced along with neutrons in the interaction
 159 between α and Be nucleus.

160 The presence of a lead shield around the sensitive volume absorbed almost completely
 161 the 59 keV photon component. A small fraction of it reached the gas through small gaps
 162 accidentally present between the lead bricks.

163 A ^{55}Fe source emitting **X-rays** with a main energy peak at 5.9 keV. This is the
 164 standard candle for calibration and performance evaluation of LEMON, and its extensive
 165 use is documented in Ref. [30].

166 Four different sets of runs have been recorded: (i) without any source and no electric
 167 signal amplification in the GEMs, to study the sensor electronic noise; (ii) without any
 168 source, but the detector fully active, to study the ambient background, mainly muons
 169 from cosmic rays and natural radioactivity; runs with either the (iii) ^{55}Fe source, to
 170 study the detector response to a known signal or with the AmBe source, to study the
 171 LEMON performances in presence of nuclear recoils.

172 Figure 4 shows images recorded with the same 30 ms exposure time, in presence
 173 of one of the two sources. The left panel shows an example of several light spots,
 174 characteristic of energy deposits due to ^{55}Fe low energy photons. The right panel shows
 175 a frame recorded in presence of the AmBe radioactive source: the short and bright track
 176 well visible in the center is very likely due to an energetic nuclear recoil induced by a
 177 neutron scattering.

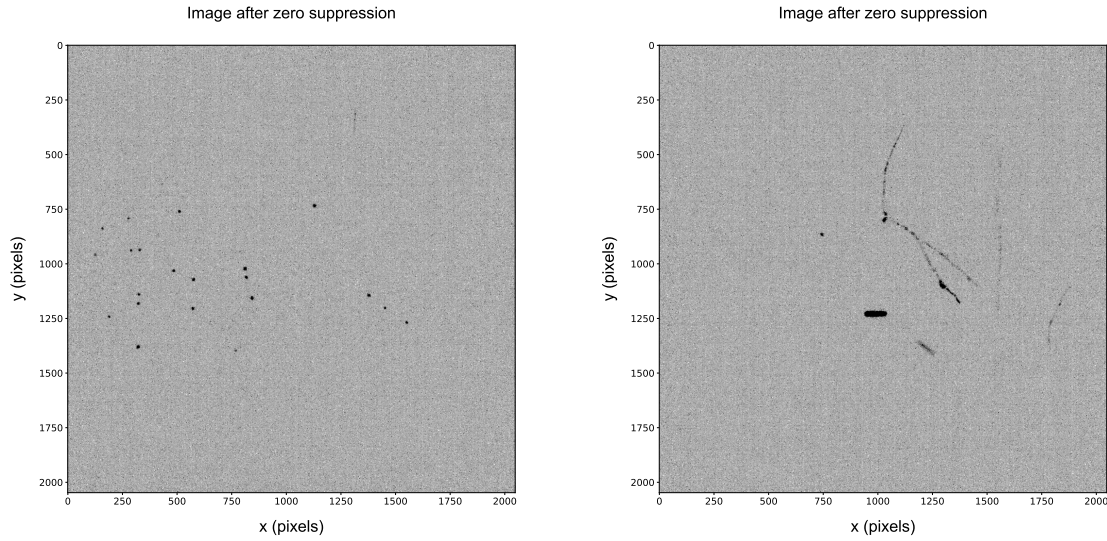


Figure 4. Two pictures taken with the sCMOS camera with a 30 ms exposure time. Left: picture taken in presence of ^{55}Fe radioactive source. Right: a nuclear recoil candidate is present, in an image with AmBe radioactive source, together with signals from natural radioactivity. The coordinates are defined such that the vertical direction is along the y-axis.

¹⁷⁸ **4. Cluster reconstruction algorithm**

¹⁷⁹ The light produced in the multiplication process through the GEMs and detected by
¹⁸⁰ the sCMOS sensor is associated in clusters of neighboring pixels. This is achieved by
¹⁸¹ following the trail of energy deposition of the particle traveling through the gas of the
¹⁸² sensitive volume. The energy released as ionization electrons is estimated by the amount
¹⁸³ of the light collected by the sensor. In the range from few keV to tens of keV for stopped
¹⁸⁴ electrons, the deposited energy is equivalent to their total kinetic energy, while for
¹⁸⁵ stopped nuclei it represent only a fraction of their initial kinetic energy. Therefore, it is
¹⁸⁶ of primary importance to have a reconstruction algorithm that includes all the camera
¹⁸⁷ pixels hit by the real photons originating from the energy deposits, while rejecting most
¹⁸⁸ of the electronic noise from the camera sensor. Noise can either create fake clusters
¹⁸⁹ or, more likely, add pixels in the periphery of clusters originated by real photons, thus
¹⁹⁰ biasing the energy estimate. Possible additional noise, arising for example from GEM
¹⁹¹ stages, was already demonstrated be negligible [30].

¹⁹² The energy reconstruction follows a three-steps procedure: the single-pixel noise
¹⁹³ suppression is briefly described in Section 4.1. This is followed by the proper clustering:
¹⁹⁴ first the algorithm to form basic clusters from single small deposits is described in
¹⁹⁵ Section 4.2, then the supercluster method, aiming to follow the full particle track, and
¹⁹⁶ seeded by the basic clusters found in the previous step, is described in Section 4.3.

¹⁹⁷ The results of this paper are based on the properties of the reconstructed
¹⁹⁸ superclusters and are described in Section 5.

¹⁹⁹ *4.1. Sensor noise suppression*

²⁰⁰ The electronic noise of the sensor was estimated in data-taking runs acquired with the
²⁰¹ sensor in complete dark, obtained by covering the camera lens with its own cap or,
²⁰² equivalently, lowering the voltage across the GEM electrodes to 300 V (*pedestal* runs).
²⁰³ The latter option, which was demonstrated to be fully equivalent to the former, is a
²⁰⁴ valuable method to measure the sensor noise periodically, and track its evolution, during
²⁰⁵ the periods without data taking of the CYGNO experiment.

²⁰⁶ For each pixel, the pedestal was computed as the average of the counts over many
²⁰⁷ frames, while the electronic noise was estimated as their standard deviation (SD). The
²⁰⁸ distribution of the pixels SD is shown in Fig. 5. The mode of this distribution is about
²⁰⁹ 1.8 photons per pixel, but a tail is present, with pixels having a noise of more than
²¹⁰ 5 photons per pixel. For such pixels, a very non-Gaussian distribution was observed,
²¹¹ while for the pixels in the bulk of the distribution, the pedestal distribution followed
²¹² a Gaussian shape. To form the pedestal-subtracted image, the pedestal mean μ_i was
²¹³ subtracted to the image for each i^{th} pixel, to account for the non-uniformity of the
²¹⁴ pedestal mean across the sensor. An initial noise suppression was applied by neglecting
²¹⁵ the pixels with counts less than 1.3SD_i . On such pedestal-subtracted zero-suppressed
²¹⁶ images an upper threshold was applied to reject hot pixels, which are more likely due to
²¹⁷ sensor instabilities than to a real energy release. They are found to be not malfunctioning

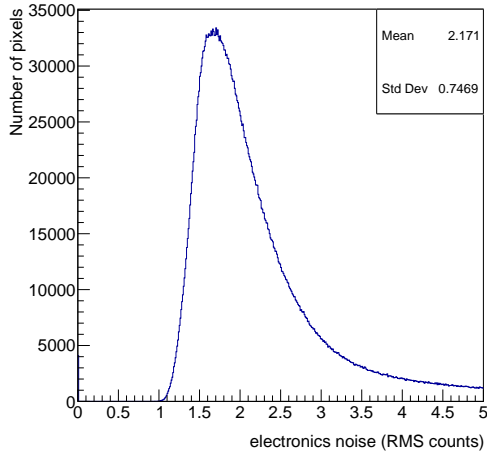


Figure 5. Distribution of the electronic noise of the sensor, estimated in images taken with sensor in complete dark, and evaluated as the SD of the distribution of the counts for each pixel.

218 pixels since they disappear after a power cycle of the camera: therefore a dynamic (run-
 219 by-run) suppression is needed. They are efficiently identified as high-intensity, isolated
 220 pixels, and distinguished by a true energy deposit, for which each pixel is surrounded
 221 by some other active pixels. A threshold is applied on the ratio R_9 between the pixel
 222 and the average of the counts in a 3×3 pixels matrix surrounding it, and a minimum
 223 number of two pixels above noise in that matrix is required to discriminate good pixels
 224 from hot ones. Only good pixels are retained for the subsequent clustering.

225 The resolution of the resulting image is initially reduced by forming *macro-pixels*, by
 226 averaging the counts in 4×4 pixel matrices. This is needed to reduce the combinatorics
 227 of the subsequent clustering algorithm, in order to be executed in a reasonable time
 228 for each image. On such 512×512 pixel map, a median filter [31] is applied, which is
 229 effective in suppressing the electronics noise fluctuations in a 4×4 pixel matrix and it is
 230 computationally efficient, as described in more details in Ref. [32]. The output image is
 231 passed to the basic clustering algorithm, described in the following.

232 4.2. Basic clusters reconstruction

233 The basic clustering algorithm, called IDBSCAN and described in details in Ref. [33],
 234 represents an improvement of the neighboring pixels clusters, called NNC, previously
 235 used to study the performance of the LEMON detector with ^{55}Fe radioactive source [30].
 236 It is briefly described also here, since it represents the seeding for the final clustering
 237 algorithm.

238 The energy deposition in the sensitive volume of the TPC is estimated from the two-
 239 dimensional (2D) projection on the $x-y$ axes of the light emitted in the multiplication
 240 process within the GEMs planes. The pattern shows a large variation, depending on the

interacting particle. For images recorded with the ^{55}Fe calibration source, the signature of the typical 5.9 keV photons is a spot of few mm^2 , with the exact size depending on the diffusion in the gas, i.e., on the distance from the anode, along z , of the point where the energy release happens (see Fig. 4 left). Muons from cosmic rays travel across the gas volume and leave a typical signature of a straight track, shown in Fig. 3 (right), but with several agglomeration with larger density along the path. Natural radioactivity shows an irregular pattern, sometimes curly, with several kinks along the path. Finally, the signal from nuclear recoils due to neutrons, originated by the AmBe source, is expected to be spot-like, or to emerge as short straight tracks with a length smaller than 1 mm for energies below 100 keV, as shown by Fig. 2.

Their track length and their size is found to depend a lot on the initial energy of the impinging neutron, and also on the mass of the recoiling nucleus in the He-CF₄ gas mixture utilized in the LEMON detector.

Thus, the clustering algorithm needs to be flexible enough to efficiently reconstruct a diverse set of patterns, from small round spots to long and kinky tracks. A first step of the clustering, called *seeding*, is used: it focuses in the clustering of spot-like neighboring pixels. The method applied for the LEMON detector is an evolution of the classic DBSCAN algorithm [34]. This is a non-parametric, density-based clustering, which groups together pixels above threshold with many neighbors, within a circle with a radius ϵ . Its distinctive characteristics making this method very suitable to the LEMON case is its ability to label as outliers, and so not to include in the clusters, pixels that lie isolated in low-density regions, i.e., pixels from electronic noise of the sensor surviving the zero suppression. The extension of DBSCAN used for LEMON data analysis consists in including a third dimension to the phase space of the points considered, adding to the pixel position (x - y coordinates) the measured number of photons in that pixel, N_{ph} . This approach improves the combinatorial background rejection and the energy resolution with respect the previously used NNC algorithm, as described in details in Ref. [33].

To be as inclusive as possible, and since different interactions may have vastly different intensities, even varying along the track, the clustering procedure is iterated three times. First, the DBSCAN parameters were tuned to form clusters of dense (in x - y dimension) and intense (in the N_{ph} dimension) pixels. The density in 3D is called *sparsity*. This step typically identifies either rare hot spots of the GEMs, or, efficiently, short nuclear recoils. The pixels belonging to the reconstructed clusters are then removed from the image, and the DBSCAN procedure is repeated, with looser sparsity parameters. The second iteration is tuned to efficiently reconstruct ^{55}Fe round spots and slices of tracks from nuclear recoils with lower intensity. It also collects the agglomeration with larger density along cosmic tracks, clearly visible in the example in Fig. 3 (right). A third iteration of DBSCAN with even looser parameters is finally executed, targeting faint portions of a cluster. These are especially used as a proxy for the characterization of clustered noisy pixels, while the first two are used as seeds for the final clustering step, described in Sec. 4.3.

To be computationally viable, the IDBSCAN basic clustering is performed on the image with reduced resolution, 512×512 . In typical images this allows the basic clusters reconstruction to be run in approximately 1 s on an Intel Xeon E5-2620 2.00 GHz and 64 GB RAM. The reconstruction algorithm is implemented in PYTHON3 [35], and interfaced with the CERN ROOT6 v.6 [36].

Examples of clustered pixels in two cases are shown in Fig. 6. The left panel shows an example of clusters reconstructed on the low-resolution image of one event with ^{55}Fe source. Three spots are clearly visible: one, as typical for events with this calibration source with a moderate activity, is reconstructed by a single cluster of the second iteration. The other two are close enough that are merged in a single cluster of the same iteration. The cases of merged spots containing twice the energy of a single X-ray deposit, given the activity of the ^{55}Fe source, represent about one tenth of the clusters in this set of runs. The energy resolution is good enough to distinguish statistically the single and merged spots, as will be described in Sec. 4.4. The optimization of the IDBSCAN parameters is done assuming a low pileup of events, typical of the running conditions for a future underground run of the CYGNO project, of which LEMON is the prototype, where the occurrences of such cases are expected to be negligible.

The right panel shows the outcome of the IDBSCAN algorithm on a longer track, presumably from natural radioactivity, and one possible short nuclear recoil. The nuclear recoil candidate is very dense, highly-energetic, and isolated. Therefore, it is reconstructed as a single cluster in the first iteration. The long track shows several clusters with higher intensity. One of them has a large energy, and it is reconstructed as an isolated single iteration-1 cluster. The rest of the track is reconstructed by multiple iteration-2 clusters, which are split where the energy deposition has a minimum extending across too many pixels to be joined together in the same cluster. Events like these, which are frequent for muons, natural radioactivity, but also signals from α -particles with higher energy, originating by the possible interaction of neutrons with the plastic material of the field cage, justify the need of the subsequent step of the *superclustering*, which follows the track without splitting it in parts. This is described in the following section.

4.3. Superclusters reconstruction

The aim of the superclustering procedure is to collect the majority of the pixels belonging to a track which is long and can be split in multiple parts in the clustering step described before. Indeed, the main limitation of IDBSCAN to follow a long track is mainly originated by the non uniform energy release along the path length. As can be clearly seen in Fig. 6 (right), or even in the example of a raw image of an event with two long cosmic rays in Fig. 3 (right), clusters with larger energy release are followed by regions along the path with a lower or even a zero release. These local minima are sometimes as large, in the 2D space, as the typical size of the ϵ parameter of DBSCAN [34]. Despite the low electronic noise of the ORCA-Flash 4.0 camera sensor, the energy releases in

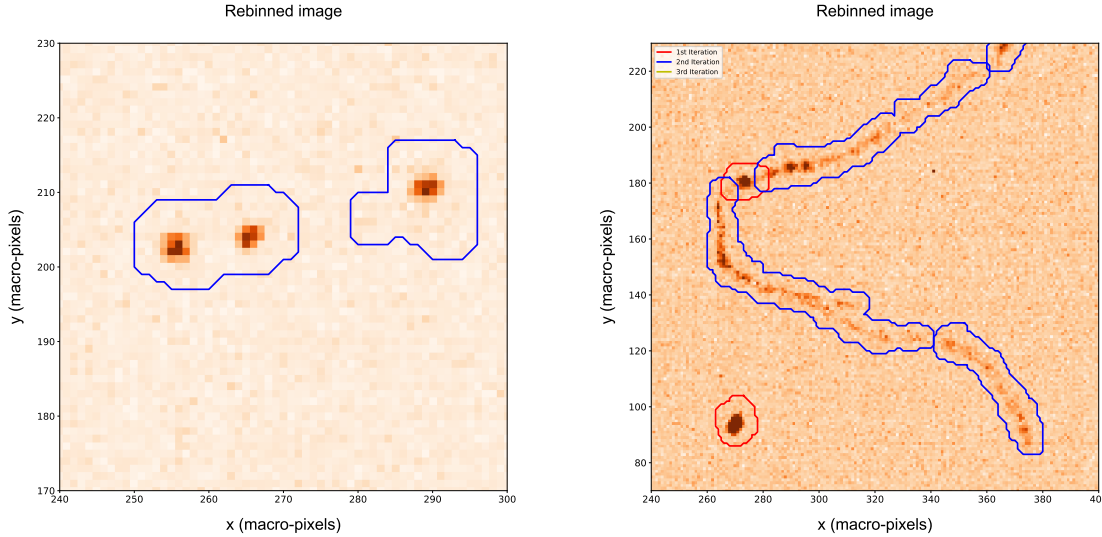


Figure 6. Basic clusters reconstructed with the IDBSCAN algorithm in the low resolution (512×512) image for two example events with very different patterns. Continuous lines represent the approximate contours of the reconstructed basic clusters of the first (red line) or second (blue line) IDBSCAN iteration. Left: clusters on spots from ^{55}Fe source, two of which are merged together. Right: Track from natural radioactivity and a nuclear recoil candidate in an event with AmBe source. The long track is split in several basic clusters of different IDBSCAN iteration.

these local minima are similar in magnitude to the average single-pixel noise.

The IDBSCAN is limited in connecting the full length of an extended path, because of two reasons. First, inflating ϵ parameter as much as needed to cover the areas of local minima conflicts with the need to reject noise around the cluster. The basic cluster parameters were optimized for the LEMON running conditions to collect most of the signals with an energy as low as few keVs and to reject the typical noise of ≈ 1 photon per pixel. This avoids collecting extra noise in the cluster, biasing the energy scale and worsening its resolution, and keeps the rate of fake clusters at a negligible level [33]. Second, the iterative nature of the algorithm, with different parameters for each iteration, each tuned for very different intensity, makes it convenient and efficient for a deposition of a fixed energy density (like the spots originating from the ^{55}Fe source), but not for the cases as in Fig. 6 (right), where the same track is split in several parts, some of them belonging to different iterations. This requires a method that can continuously follow the pattern of the track, profiting of the full resolution image, where the gradients of the energy deposition along the track trajectory are smaller than the ones in the transverse direction, but still give information on the energy release pattern. Several existing algorithms were tested to profit of this, but executing any of them on the full 2048×2048 image is not manageable CPU-wise, due to the huge pixel combinatorics.

Therefore, the procedure adopted for the final supercluster reconstruction in the LEMON detector starts from defining the *interesting regions* in the image that may

343 contain pixels from an energy deposit. These are identified by the basic cluster algorithm
 344 IDBSCAN previously described, which is applied on the 512×512 reduced-resolution
 345 image. In order to gather the peripheral pixels, especially along the track trajectory
 346 where breaks into small basic clusters may have happened, a window of 5×5 pixels is
 347 considered, around each pixel belonging to a macro-pixel clustered in a basic cluster.
 348 A full resolution image formed only by the interesting pixels passing the simple initial
 349 filtering described in Sec. 4.1 is created. The gradients of the intensity N_{ph} in such
 350 image are computed pixel-by-pixel to look for the edge region where the image turns
 351 from signal to noise-only:

$$352 \quad ||\nabla(N_{ph})|| = \sqrt{\left(\frac{\partial N_{ph}}{\partial x}\right)^2 + \left(\frac{\partial N_{ph}}{\partial y}\right)^2}, \quad (2)$$

353 while the gradient direction is given by:

$$354 \quad \theta = \tan^{-1} \left(\frac{\partial N_{ph}}{\partial y} / \frac{\partial N_{ph}}{\partial x} \right). \quad (3)$$

355 In order to reduce the effect of the noise, which induces fluctuations in the first
 356 derivatives of Eq. 2, a Gaussian filter is applied, which smoothen the response by
 357 convolving the pixel intensity with a Gaussian function, having as σ the SD of the
 358 intensities of all the pixels considered, and rejecting the ones falling outside a 5σ window.

359 The superclustering algorithm, applied on the filtered image, is an application of the
 360 *morphological geodesic active contours* [37,38], called GAC in the following. This method
 361 uses an active contour finding, widely used in computer vision, where the boundary curve
 362 \mathcal{C} of an object is detected by minimizing the *energy* E associated to \mathcal{C} :

$$363 \quad E(\mathcal{C}) = \int_0^1 g(N_{ph})(\mathcal{C}(p)) \cdot |\mathcal{C}_p| dp, \quad (4)$$

364 where $ds = |\mathcal{C}_p| dp$ is the arc-length parameterization of the curve in the 2D space, and
 365 g is the stopping edge function, which allows to select the boundary of the cluster. In
 366 the GAC method used for the LEMON images, the g function is purely geometrical, and
 367 uses the geodesics of the image, i.e., the local minimal distance path joining points with
 368 the same light intensity gradient. The function $g(N_{ph})$ is given by:

$$369 \quad g(N_{ph}) = \frac{1}{\sqrt{1 + \alpha |\nabla G_\sigma * N_{ph}|}}, \quad (5)$$

370 which is minimal in the edges of the image. The $G_\sigma * N_{ph}$ is the aforementioned 5σ
 371 Gaussian filter, and the parameter α , which regulates the strength of the filter, was
 372 tuned on typical LEMON images to be $\alpha = 100$.

373 This method was chosen because it allows to follow patterns that may vary from
 374 convex to concave shape, eventually with kinks, e.g. in cases of δ -ray emissions. To
 375 improve the shrinking of the cluster boundary in the cases of tracks turning from
 376 concave to convex along their trail, the *balloon* force [38], which is a term added to
 377 Eq. 4 to smooth the cluster contour, is set to -1, in order to push the contour towards a
 378 border in the areas where the gradient is too small. A number of 300 iterations is used
 379 to evolve the supercluster contour.

380 The example track shown in Fig. 6 (right) after the basic clustering step, is shown
 381 again in full resolution, zoomed around the cluster, in Fig. 7 (left). The output of
 382 the superclustering with the GAC algorithm is shown on the right panel of the same
 383 figure. The splitting of the cluster, happening at the basic clusters step, is recovered:
 384 the portions with high and low density along the path of the energy release are joined
 385 together. Other three examples of superclustered images are shown in Fig. 8, in runs
 386 without any artificial radioactive source. The top left panel shows an example of a
 387 cosmic ray track fully reconstructed by the GAC superclustering, which also includes
 388 a δ -ray in the middle of the track length. The top right panel shows an example of
 389 curly track from a candidate of natural radioactivity interaction; bottom panel shows
 390 an example where both a cosmic ray and a curly track are present. In this case, the
 391 extremes of the long and straight track are still split, but this is much rarer than after
 392 the basic clustering, and it happens when the local minima along the trajectories are
 compatible with noise-only for more than ≈ 1 cm.

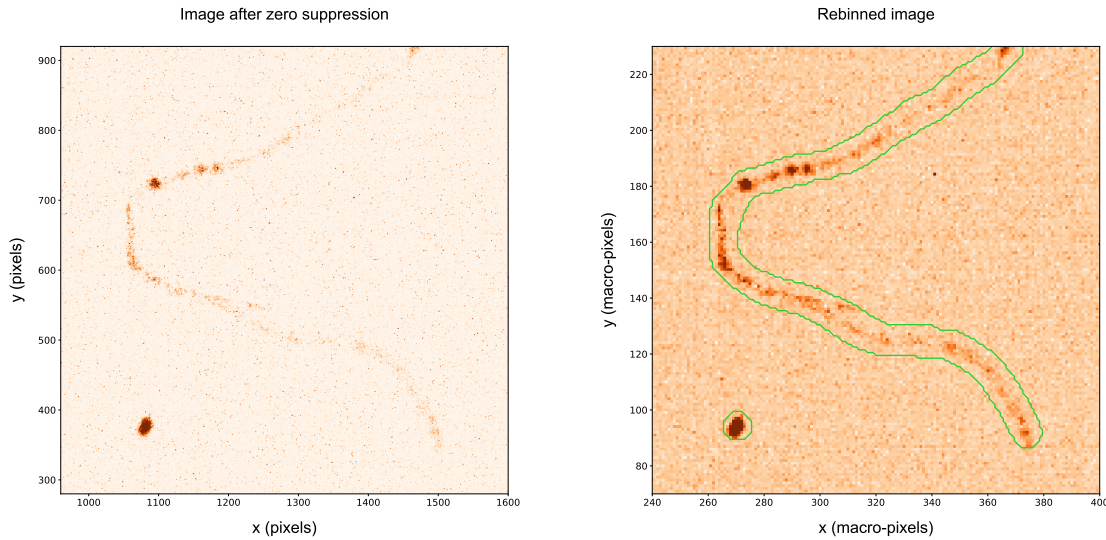


Figure 7. Left: zoom on the full-resolution image of a track candidate in a run with the AmBe radioactive source. Right: output of the superclustering on the rebinned image. The continuous line represents the approximate contour of the reconstructed supercluster.

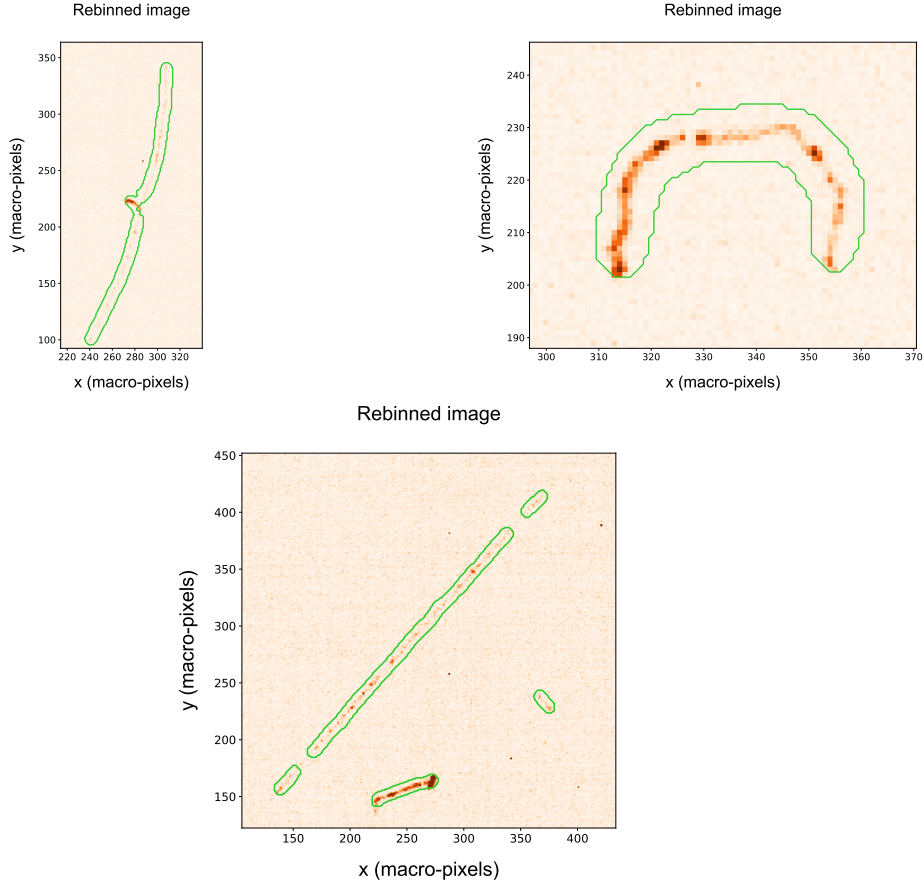


Figure 8. Superclusters reconstructed in a run without artificial radioactive sources. The continuous lines represent the approximate contours of the reconstructed superclusters. Top left: cosmic ray track fully reconstructed by the GAC superclustering. A δ -ray is included in the supercluster. Top right: curly track from a candidate of natural radioactivity interaction. Bottom: a cosmic ray with the extremes not joined to the main track, plus a curly track from natural radioactivity.

394 *4.4. Energy scale calibration using ^{55}Fe source*

395 The containment of the energy in the supercluster was verified with simulations of
 396 nuclear and electron recoils within the gas mixture of the LEMON detector, performed
 397 with SRIM [29]. For both types of recoils, for the energy range of interest for DM search,
 398 i.e., $E \lesssim 100$ keV, when considering deposits without electronics noise and no diffusion
 399 in the gas, the peak of the $|E - E_{\text{true}}|/E_{\text{true}}$ distribution is within 5%. Adding a noise
 400 approximated as a Gaussian function with a mean and a SD equal to the ones observed
 401 in the pedestal runs, and a diffusion following the parameterization in Eq. 1, the fraction
 402 of the true energy contained in the supercluster decreases to about 80%. The decrease in
 403 the energy containment in the supercluster is due to the smearing of the 2D track pattern
 404 around the periphery of the cluster, mostly due to the diffusion effect. This decreases the
 405 gradients in Eq. 2 around the edges, and so the supercluster can shrink more around the
 406 crest, loosing part of the tails that can be confused more easily with the noise. A more
 407 realistic noise description, and an improved diffusion model, based on the one measured
 408 in data is necessary to tune the supercluster parameters in simulation to recover part
 409 of the containment. The energy resolution found in simulation (around 4%) is far from
 410 the measured one in data, around 18%, because of the absence, in the simulation, of
 411 the dominant contribution of the response fluctuations: Poissonian distribution of the
 412 number of primary electrons ionized in the gas and exponential behavior of the number
 413 of secondary electrons produced in each GEM amplification stage [16]. Both of them are
 414 expected to give rise to fluctuations of the order to 10%, that, once added in quadrature,
 415 can account for a large part of the measured energy resolution.

416 The absolute energy scale was then calibrated with the energy distribution measured
 417 in data with the ^{55}Fe source, which provides monochromatic photons of 5.9 keV, with
 418 the procedure described in Ref. [30]. The supercluster integral is defined as:

$$419 \quad I_{SC} = \sum_i^{\text{cluster}} N_{ph}^i, \quad (6)$$

420 where N_{ph}^i is the number of counts (photons) in the i^{th} pixel, and the sum runs over
 421 all the pixels of the supercluster. While to perform the basic- and super-clustering only
 422 pixels passing the zero suppression are considered, for the energy estimate in Eq. 6 all
 423 the pixels within the cluster contours are counted, eventually having negative N_{ph}^i after
 424 the pedestal subtraction. This choice is meant to avoid a bias on the energy estimate,
 425 since after the pedestal subtraction the distribution of the noise is centered around zero.
 426 The distribution of I_{SC} , for a run taken in presence of ^{55}Fe source, is shown in Fig. 9. In
 427 addition to the main peak, with a mean of about 2500 counts, a broader peak is clearly
 428 distinguished, which represents the cases of two merged spots, with an integral twice
 429 the single spot one. An example of such a merged spot is given in Fig. 6 (left). The
 430 position of the maximum in the single-spot distribution in runs with ^{55}Fe source allowed
 431 to calibrate the absolute energy scale of the LEMON detector. The energy resolution
 432 for the reconstructed GAC superclusters is about 18%, similar to the one that can be

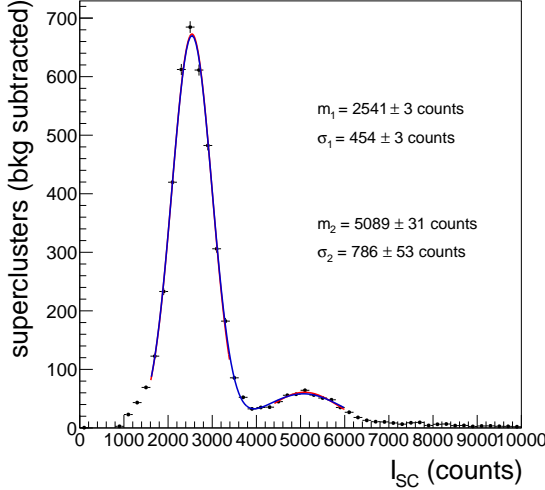


Figure 9. Distribution of the supercluster integral, before the absolute energy scale calibration is applied, in events with the ^{55}Fe source. Clearly visible is the large peak of a single spot, and, at around twice the energy, a broader peak for the case of two neighboring spots merged in a single supercluster.

433 obtained with only the basic clustering step with IDBSCAN [33], and improving the one
 434 with the simple NNC algorithm previously used [30].

435 Using runs with this monochromatic, high rate source, positioned at different
 436 distances from the GEM planes, a decrease of the light response for lower distances
 437 from the GEM was observed. This effect is opposite to the expected behavior of a
 438 lower light yield at larger distances. Indeed, it is expected that, during the drift along
 439 the z -direction, the ionization charge undergoes a diffusion in the TPC gas, and some
 440 electrons are removed by attachment to the gas molecule. Consequently, some loss in the
 441 light collection may be expected. The opposite behavior, instead, is clearly observed.
 442 While this effect is currently under study in more detail, it was attributed to a possible
 443 saturation effect of the GEMs, especially in the third stage of multiplication, where
 444 the charge density in one GEM hole is maximal. Under this hypothesis, an effective,
 445 empirical correction was developed, which relies on the charge density of a cluster from
 446 a ^{55}Fe deposit. The light density, δ , is defined as:

$$447 \quad \delta = I_{SC}/n_p, \quad (7)$$

448 where n_p is the number of pixels passing the zero-suppression threshold (differently
 449 from the definition of I_{SC} , where all the pixels in the supercluster are considered). This
 450 effective calibration returns the absolute energy of a spot-like region, similar in size
 451 to the ^{55}Fe clusters, as a function of the supercluster density, δ : $E = c(\delta) \cdot I_{SC}$. In
 452 the hypothesis of saturation, the *local* density along the track is the parameter which
 453 regulates the magnitude of the effect, thus the correction has to be applied dynamically
 454 for slices of the supercluster having a size similar to the ^{55}Fe spots. This is achieved

455 with the procedure described in the following.

456 First, the supercluster *skeleton*, i.e., the 1-pixel-wide representation along the path,
 457 is reconstructed. This is achieved through a morphological thinning of the superclusters
 458 with the iterative algorithm from Ref. [39,40]. Second, a pruning of the obtained skeleton
 459 is done, to remove residual small branches along the main pattern, using a hit-or-miss
 transform. The output of this process for one example track is shown in Fig. 10. For

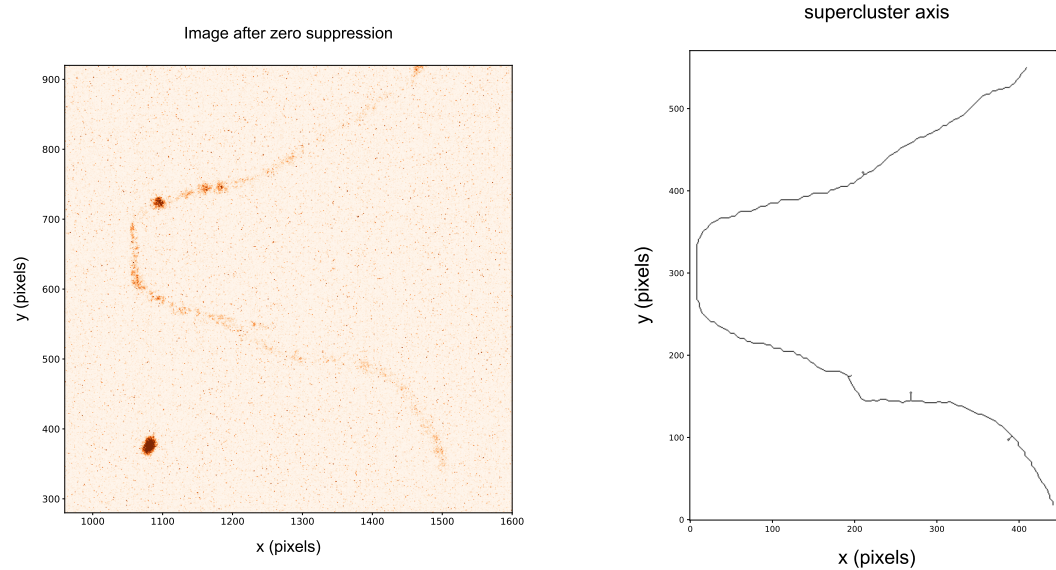


Figure 10. Left: zoom on the full-resolution image of a track candidate in a run with the AmBe radioactive source. Right: output of the skeletonization and pruning of the branches for one example supercluster extended in space.

460
 461 the calibration procedure, the found skeleton is followed, starting from one of the two
 462 end points, and circles having their center on a pixel of the skeleton and their radius
 463 equal to the average spot size of the ^{55}Fe clusters are defined. It was checked that
 464 this procedure includes all the pixels of the original cluster for the vast majority of the
 465 clusters considered. The local density δ_s of the slice s is computed, and its integral
 466 I_s is calibrated to an absolute energy through the effective correction $E_s = c(\delta_s) \cdot I_s$.
 467 The pixels of the supercluster used for the slice calibration are removed (including the
 468 skeleton ones), and the procedure is iterated, until having included all the pixels. The
 469 sum of the energies of all the slices is the estimate of the calibrated energy of the
 470 supercluster:

$$471 \quad E_{SC} = \sum_s^{slices} E_s \quad (8)$$

472 As a closure test of this procedure, the calibrated energy of the superclusters
 473 reconstructed in the runs with the ^{55}Fe source is obtained. The value of the energy
 474 peak was obtained by fitting the distribution with the same function used in Fig. 9, and
 475 equals to $m_1 = 5.93 \pm 0.01$ keV, compatible with the expected value. The calibration

procedure is an overkill for the case of the small ^{55}Fe spots, but it is necessary for very long cosmic ray tracks or even for medium-length superclusters from nuclear and electron recoils. The energy resolution worsen after the calibration ($\sigma_1 = 1.48 \pm 0.01$, i.e., 25% energy resolution), as a sign that the empiric correction is still suboptimal.

The skeletonization procedure provides a general method to estimate the track length (l_p), accurate both in the case of straight and curving track. As a check, it has been verified that, in the case of straight tracks, the length extracted in this way coincides with the one of the major axis estimated with a singular value decomposition (SVD), described in the following section. For exactly round spots, the skeleton would collapse in the center of the cluster and the resulting length would be 1 pixel, but this completely symmetric case never happens in the considered samples.

5. Cluster shape observables

The interaction of different particles with the nuclei or the electrons in the gas of the TPC produces different patterns of the 2D projection of the initial 3D particle trajectory. These characteristics, to which we refer generically as *cluster shapes observables*, are useful to discriminate different ionizing particles. In particular, they were used to select a pure sample of nuclear recoil candidates produced by the interaction of the neutrons originating from the AmBe source and to identify various sources of backgrounds. The main cluster shape observables are described in the following:

- *projected length and width*: a SVD on the $x \times y$ matrix of the pixels belonging to the supercluster is performed. The eigenvectors found can be interpreted as the directions of the two axes of an ellipse in 2D. The eigenvalues represent the magnitudes of its semiaxes: the major one is defined as *length*, l the minor one as *width*, w . These are well defined for elliptic clusters, or for long and straight tracks. The directions along the major and the minor axis are defined as *longitudinal* and *transverse* in the following. The longitudinal and transverse supercluster profiles, for the cosmic ray track candidates shown as an example in Fig. 8 (bottom) are shown in Fig. 11. The longitudinal profile shows the typical pattern of energy depositions in clusters, while the transverse profile, dominated by the diffusion in the gas, shows a Gaussian shape. It has to be noted that the cluster sizes represent only the projection of the 3D track in the TPC on the 2D $x-y$ plane;
- *projected path length*: for curly and kinky tracks the values returned by the SVD of the supercluster are not an accurate estimates of their size. While the width is dominated by the diffusion, the length for patterns like the one shown in the example of Fig. 7 is ill-defined. Thus, the more general path length, l_p , computed with the skeletonization procedure in Fig. 10 is used to estimate the linear extent for both straight and curved tracks.
- *Gaussian width*: the original width of the track in the transverse direction is expected to be much lower than the observed width induced by the diffusion in

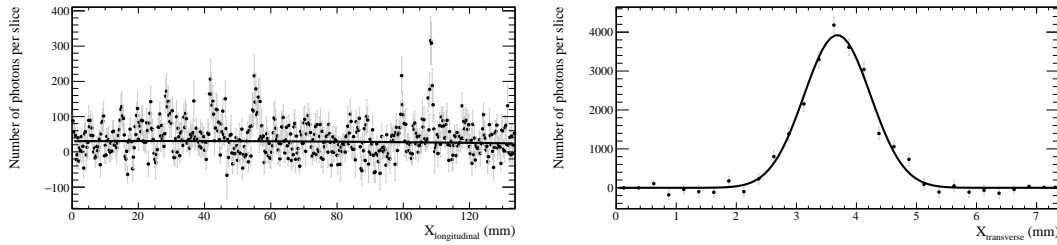


Figure 11. Supercluster profile in the longitudinal (top) or transverse (bottom) direction, for a long and straight cosmic ray track candidate shown in Fig. 8 (bottom). The longitudinal profile shows an energy deposition in sub-clusters, while the transverse direction shows the typical width of the diffusion in the gas. For the longitudinal profile, the line represent the average number of photons per slice. For the transverse profile, it represents a fit with a Gaussian PDF.

the gas. Thus, as shown in Fig. 11 (right), the standard deviation, σ_{Gauss}^T , can be estimated by a fit with a Gaussian probability density function (PDF);

- *slimness*: the ratio of the width over the path length, $\xi = w/l_p$, represents the aspect ratio of the cluster. It is very useful to discriminate between cosmic rays-induced background (long and thin) from low energy nuclear or electron recoils (more elliptical or round, as the ^{55}Fe spots);
- *integral*: the total number of photons detected by all the pixels gathered in the supercluster, I_{SC} , as defined in Eq. 6;
- *pixels over threshold*: the number of pixels in the supercluster passing the zero-suppression threshold, n_p ;
- *density*: the ratio δ of I_{SC} , divided by n_p , as defined in Eq. 7;
- *energy*: the calibrated energy, expressed in keV. The calibration method simultaneously performs both the per-slice correction as a function of the local δ , and the absolute energy scale calibration, which corrects the non perfect containment of the cluster, i.e., the bias in the distribution of E/E_{true} , using with ^{55}Fe source.

The projected supercluster path length, l_p , and Gaussian transverse size, σ_{Gauss}^T , are shown in Fig. 12, for data taken in different types of runs. During the data-taking approximately 3000 frames were recorded in absence of any external radioactive source (*no-source* sample). In these frames the interaction of ultra-relativistic cosmic ray particles (mostly muons) are clearly visible as very long clusters. Internal radioactivity of the LEMON materials also contribute with several smaller size clusters. About 1500 frames were acquired with the AmBe source, and approximately 10^4 calibration images with ^{55}Fe source. In Fig. 12, as well as in the following ones showing other cluster properties, the distributions obtained in runs without radioactive sources are normalized to the AmBe data total CMOS exposure time. For the data with ^{55}Fe source, since the activity of the source is such to produce about 15 clusters/event, the data are scaled by

a factor one-tenth with respect to the AmBe exposure time for clearness. Considerations about the trigger efficiency scale factor between data with and without an radioactive source are detailed later. The distributions in this section aim to show the different cluster shape observables among the different kinds of events.

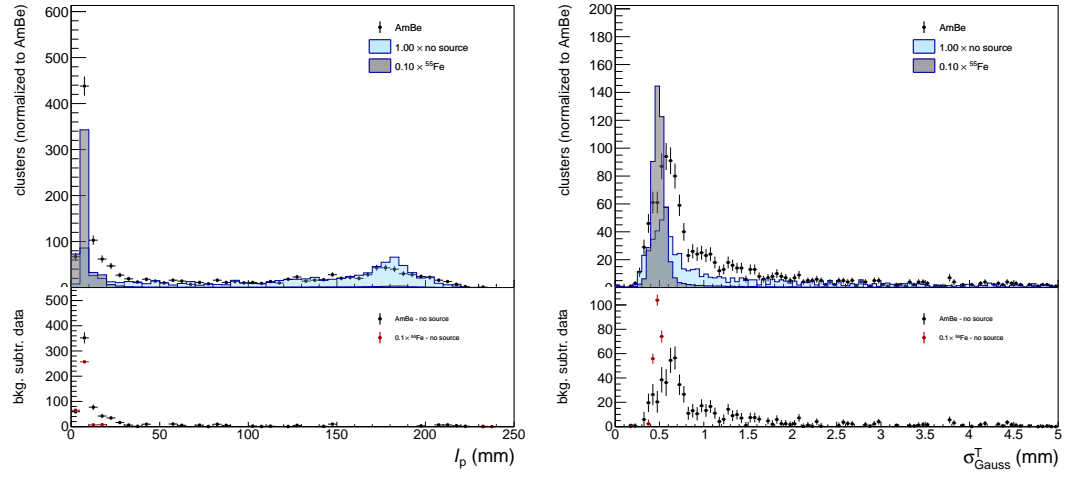


Figure 12. Supercluster sizes projected onto the x - y plane. Left: longitudinal path length, l_p . Right: transverse Gaussian spread, σ_{Gauss}^T . Filled points represent data with AmBe source, dark gray (light blue) distribution represents data with ^{55}Fe source (no source). The normalization of data without any radioactive source is scaled to the same exposure time of the AmBe one. For the data with ^{55}Fe source , a scaling factor of one tenth is applied for clearness, given the larger activity of this source.

Figure 12 shows the cluster sizes distributions in the longitudinal and transverse directions for different sets of runs. Data show an average Gaussian width for the ^{55}Fe spots $\sigma_{Gauss}^T \approx 500 \mu\text{m}$ (dominated by the diffusion in the gas), while it is larger, approximately $625 \mu\text{m}$, for data with AmBe source. The contribution of cosmic rays, present in all the data, is clearly visible in the data without any radioactive source, corresponding to clusters with a length similar to the detector transverse size (22 cm).

Other observables are the slimness, ξ , and the light density, δ , shown in Fig. 13. The former is a useful handle to reject tracks from cosmic rays, which typically have a slim aspect ratio, i.e., low values of ξ , while the clusters from ^{55}Fe are almost round, with values $0.9 \lesssim \xi < 1$. By construction, $\xi < 1$, since the width is computed along the minor axis of the cluster, and for round spots it peaks at around 0.9. The apparent threshold effect is purely geometrical, due to the minimal size of the macro-pixel (4×4) used at the basic clustering step which can be larger than a round spot from ^{55}Fe . Data with AmBe source, which contains a component of nuclear recoils, show a component of round spots, similar in size to the ones of ^{55}Fe , and a more elliptical component, with $0.4 < \xi < 0.8$ values. Finally, the light density, δ , is the variable expected to better discriminate among different candidates: cosmic rays induced background, electron recoils and nuclear recoil candidates. This is the variable used in this paper

for the final particle identification. The identification results can be improved using additional cluster shape variables, also profiting of their different correlations for signal and background clusters, via a multivariate approach, but here priority is given to the straightforwardness, rather than the ultimate performance.

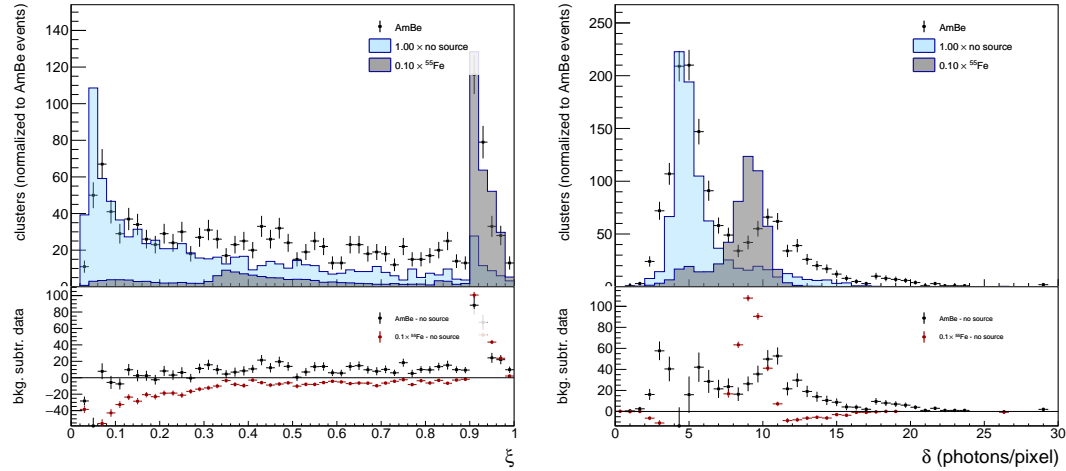


Figure 13. Supercluster variables. Left: slimness ξ ; right: light density δ . Filled points represent data with AmBe source, dark gray (light blue) distribution represents data with ^{55}Fe source (no source). The normalization of data without source is to the same exposure time of the AmBe one. For the data with ^{55}Fe , a scaling factor of one tenth is applied for clearness, given the larger activity of this source.

Finally, Fig. 14 (left) shows the calibrated energy (E) spectrum for the reconstructed superclusters. The energy spectrum shows the $E = 5.9\text{ keV}$ peak in the first bin of the distribution for data with ^{55}Fe source, and the expected broad peak for minimum ionizing particles traversing the $\approx 20\text{ cm}$ gas volume at around 60 keV . The distribution of the observed average projected $\frac{dE}{dl_p}$ for the no-source sample and for the AmBe samples is shown in Fig. 14 (right). The broadening of the distribution is mainly due to the specific energy loss fluctuation in the gas mixture of the cosmic ray particles. Its modal value, corrected for the effect of the angular distribution (an average inclination of 56° was measured from track reconstruction) is 2.5 keV/cm , in good agreement with the GARFIELD prediction of 2.3 keV/cm .

5.1. Background normalization

The data with AmBe source, taken on the Earth surface, suffers from a large contribution of interactions of cosmic rays, and from ambient radioactivity, whose suppression is not optimized for the LEMON detector. The cluster shape observables provide a powerful handle to discriminate them from nuclear recoils candidates, but the small residual background needs to be statistically subtracted. The distributions shown earlier, where the different types of data are normalized to the same exposure time, demonstrate that

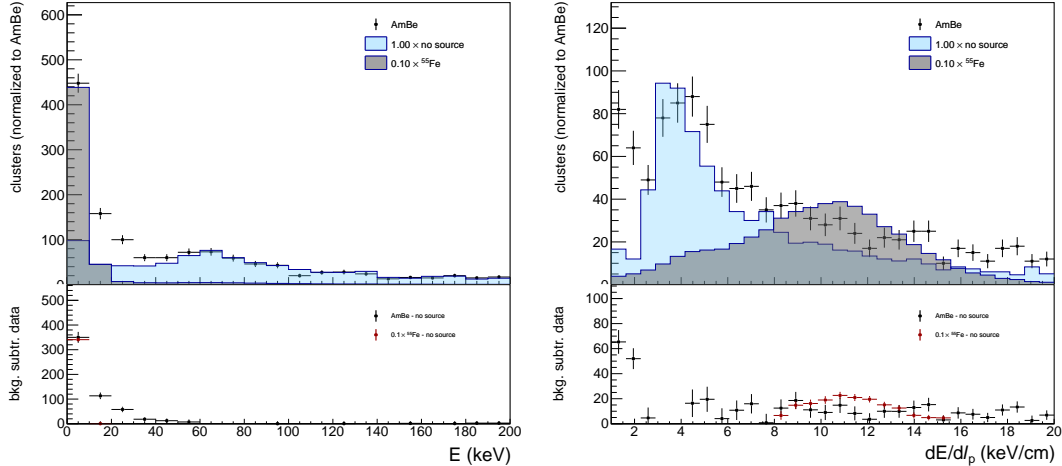


Figure 14. Supercluster calibrated energy spectrum (left) and their average $\frac{dE}{dl_p}$. Filled points represent data with AmBe source, dark gray (light blue) distribution represents data with ^{55}Fe source (no source). The normalization of data without source is to the same exposure time of the AmBe one. For the data with ^{55}Fe , a scaling factor of one tenth is applied for clearness, given the larger activity of this source.

the live-time normalization provides already a good estimate of the amount of cosmic rays in data with radioactive sources. This approach does not account for a possible bias from the trigger, which is generated by the PMT signals, as described in Sec. 2. Indeed, in runs with the AmBe source, the PMT can trigger both on signals from neutron recoils or photons produced by the ^{241}Am , and on ubiquitous signals from cosmic rays, while in the sample without source only the latter are possible. Therefore, during the same exposure time, the probability to trigger on cosmic rays is lower in events with AmBe than in no-source events. The trigger efficiency scale factor, ε_{SF} , can be obtained as the ratio of the number of clusters selected in pure control samples of cosmic rays (CR) obtained on both types of runs:

$$\varepsilon_{SF} = \frac{N_{CR}^{AmBe}}{N_{CR}^{no-source}}. \quad (9)$$

The CR control region is defined by selecting clusters with $l > 13\text{ cm}$, $\xi < 0.1$, $\sigma_{Gauss}^T < 6\text{ mm}$, and having an energy within a range dominated by the cosmic rays contribution, $50 < E < 80\text{ keV}$. The selected clusters show small values of $\delta \approx 5$, well compatible with the small specific ionization of ultra-relativistic particles. This sample is limited in statistics, but it is expected to be almost 100% pure. The scale factor obtained is $\varepsilon_{SF} = 0.75 \pm 0.02$.

In Fig. 15 the typical light density and polar angle (with respect the horizontal axis) distributions for long clusters of any energy, still dominated by cosmic rays, are shown for the AmBe and for the no-source sample, after having applied the ε_{SF} scale factor to the latter. Clusters with $\delta < 6$ are thus expected to be mostly coming from muon tracks, and they show indeed a polar angle which is shifted at values towards 90° .

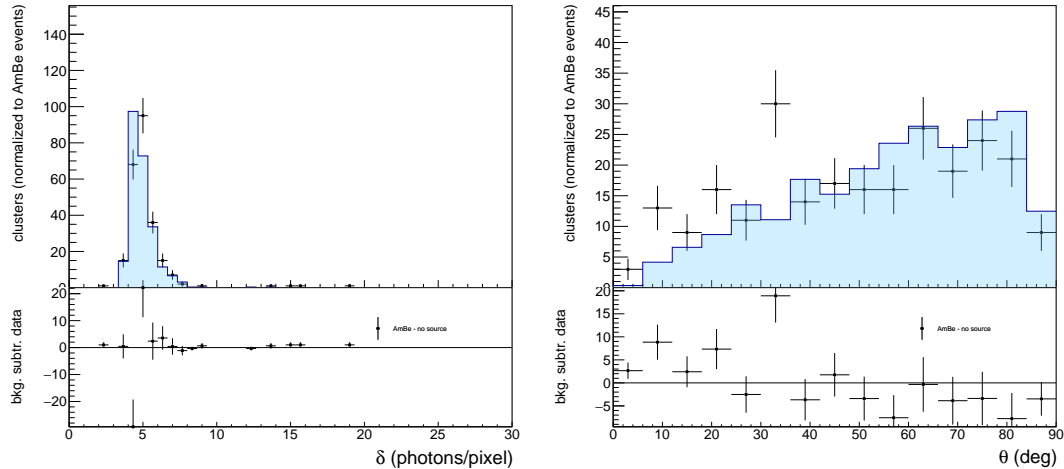


Figure 15. Supercluster light density δ (left) and polar angle (right) - with respect to the horizontal axis - distributions for long clusters, dominated by cosmic rays tracks. Filled points represent data with AmBe source, light blue distribution represents data without any radioactive source. The normalization of data without source is to the same exposure time of the AmBe one, accounting for the trigger scale factor ε_{SF} , as defined in the text.

607 6. Nuclear recoil identification results

608 As mentioned in the previous Section, the 1D observable chosen to distinguish the signal
 609 of nuclear recoils from the various types of background is the energy density δ of the
 610 cluster.

611 6.1. Signal preselection

612 To enhance the purity of the signal sample, a preselection was applied, prior to a tighter
 613 selection on δ : clusters with $l_p > 6.3$ cm or $\xi < 0.3$ were rejected to primarily suppress
 614 the contribution from cosmic rays. A further loose requirement $\delta > 5$ photons/pixel was
 615 also applied to remove the residual cosmic rays background based on their low specific
 616 ionization. These thresholds, which only reject very long and narrow clusters, are very
 617 loose for nuclear recoils with $E < 1$ MeV energies, given the expected range in simulated
 618 events, shown in Fig. 2, of less than 1 cm. Thus the preselection efficiency for signal
 619 is assumed to be 100%. For electron recoils it can be estimated on data by using the
 620 ^{55}Fe data sample, and is measured to be $\varepsilon_B^{\text{presel}} = 70\%$. Since the X-ray photo-electrons
 621 of this source are monochromatic, the estimate of the electron recoils rejection is only
 622 checked for an energy around $E = 5.9$ keV. The spectrum of nuclear recoils from AmBe
 623 source, instead, extends over a wider range of energies, around [1–100] keV.

624 With this preselection, the distribution in the 2D plane $\delta-l_p$ is shown in Fig. 16 for
 625 AmBe source and no-source data and for the resulting background-subtracted AmBe
 626 data. The latter distribution shows a clear component of clusters with short length

($l_p \lesssim 1$ cm) and high density ($\delta \gtrsim 10$), expected from nuclear recoils deposits.

In addition, it shows a smaller component, also present only in the data with AmBe source, of clusters with a moderate track length, $1.5 \lesssim l_p \lesssim 3.0$ cm, and a lower energy density than the one characteristic of the nuclear recoils ($9 \lesssim \delta \lesssim 12$). Since the density is inversely proportional to the number of active pixels n_p , which is correlated to the track length, the almost linear decrease of δ as a function of l_p points to a component with fixed energy. The ^{241}Am is expected to produce photons with $E = 59$ keV. This hypothesis is verified by introducing an oblique selection in the $\delta - l_p$ plane: $|\delta - y| < 2$, where $y = 14 - p_l/50$, for the clusters with $120 < l_p < 250$ pixels, defining the *photon control region, PR*. The approximate oblique region in the $\delta - l_p$ plane corresponding to *PR* is also shown in Fig. 16. The obtained energy spectrum for these clusters is shown in Fig. 17, which indeed shows a maximum at $E = 60.9 \pm 3.6$ keV, within the expected resolution. These events are thus rejected from the nuclear recoils candidates by vetoing the *PR* phase space.

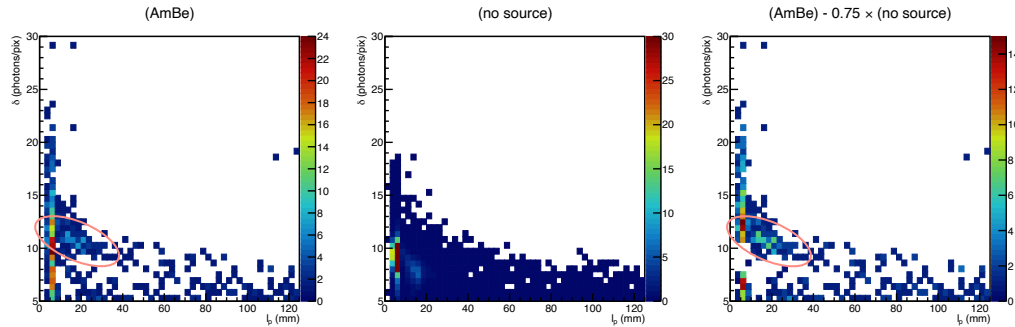


Figure 16. Supercluster light density δ versus length l_p , for data with AmBe source (left), data without any artificial source (middle), and the resulting background-subtracted AmBe data. The normalization of data without source is to the same exposure time of the AmBe one, accounting for the trigger scale factor ε_{SF} , as defined in the text. The orange ellipse represents the approximate contour of the 59 keV photons control region (*PR*) defined in the text.

6.2. PMT-based cosmic ray suppression

An independent information to the light detected by the sCMOS sensor of the camera is obtained from the PMT pulse, used to trigger the image shooting. For each image acquired, the corresponding PMT pulse waveform is recorded. Tracks from cosmic rays, which typically have a large angle with respect the cathode plane, as shown in Fig. 15 (right), show a broad PMT waveform, characterized by different arrival times of the several ionization clusters produced along the track at different z . Conversely, spot-like signals like ^{55}Fe deposits or nuclear recoils are characterized by a short pulse, as shown in Fig. 18.

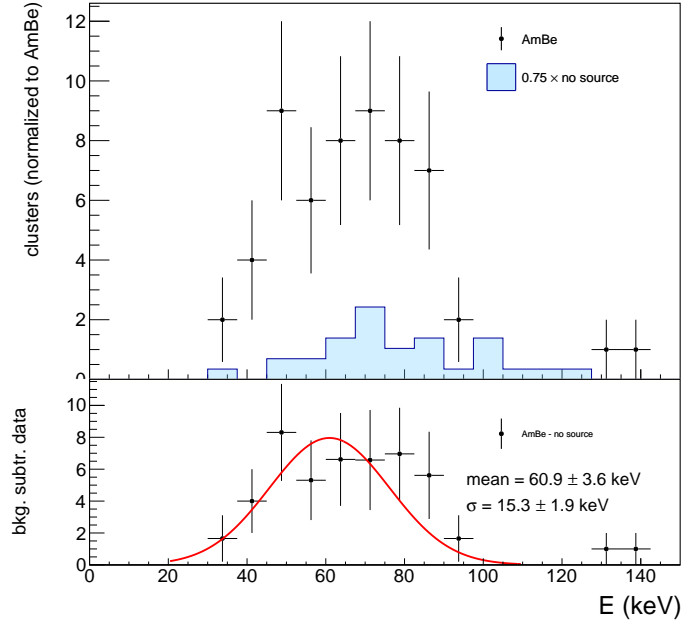


Figure 17. Calibrated energy spectrum for candidates in the control region PR , defined in the text. The background-subtracted distribution is fitted with a Gaussian PDF, which shows a mean value compatible with $E = 59$ keV originated from the ^{241}Am γ s interaction within the gas.

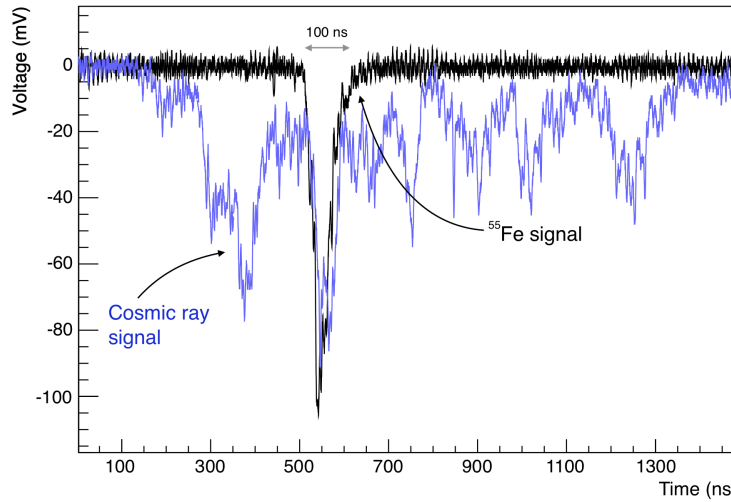


Figure 18. Example of two acquired waveforms: one short pulse recorded in presence of ^{55}Fe radioactive source, together with a long signal very likely due to a cosmic ray track.

650 The Time Over Threshold (TOT) of the PMT pulse was measured, and is shown in
 651 Fig. 19. It can be seen from the region around 270 ns, dominated by the cosmic rays also

652 in the data with the AmBe source, that the trigger scale factor ε_{SF} also holds for the PMT event rate. As expected, spot-like clusters (in 3D) correspond to a short pulse in

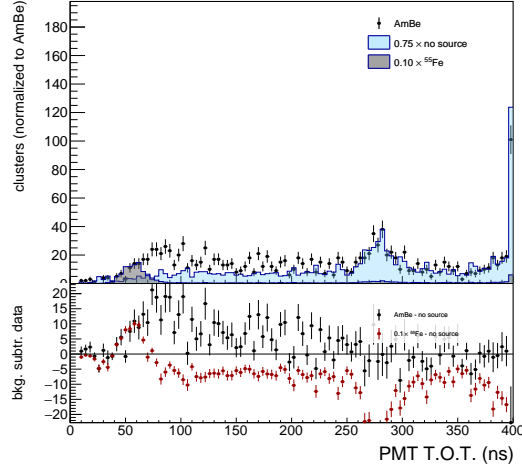


Figure 19. PMT waveform time over threshold (TOT). The last bin integrates all the events with $TOT > 400$ ns. Filled points represent data with AmBe source, dark gray (light blue) distribution represents data with ^{55}Fe source (no source). The normalization of data without source is to the same exposure time of the AmBe one, with trigger scale factor ε_{SF} applied. For the data with ^{55}Fe , a scaling factor of one tenth is applied for clearness, given the larger activity of this source.

653
654 the PMT, while cosmic ray tracks have a much larger pulse. The contribution of cosmic
655 ray tracks is clearly visible in the data with radioactive sources. A selection on this
656 variable is helpful to further reject residual cosmic rays background present in the AmBe
657 or ^{55}Fe data, in particular tracks which may have been split in multiple superclusters,
658 like the case shown in Fig. 8 (bottom), and thus passing the above preselection on the
659 cluster shapes. A selection $TOT < 250$ ns is then imposed. It has an efficiency of 98% on
660 cluster candidates in AmBe data (after muon-induced background subtraction), while
661 it is only 80% efficient on data with ^{55}Fe source. This larger value is expected because
662 of the residual contamination of signals from cosmic rays, which fulfill the selection
663 because their track is split in multiple sub-clusters, or because they are only partially
664 visible in the sCMOS sensor image. These can be eventually detected as long, in the time
665 dimension, by the PMT. The light density and the energy spectrum of the preselected
666 clusters are shown in Fig. 20.

667 6.3. Light density and ^{55}Fe events rejection

668 The light density distribution, after the above preselection and cosmic ray suppression,
669 appear to be different among the data with AmBe source, data with ^{55}Fe source, and
670 data without any artificial source. The cosmic-background-subtracted distributions
671 of δ in AmBe data and ^{55}Fe data, shown in the bottom panel of Fig. 20 (left), are

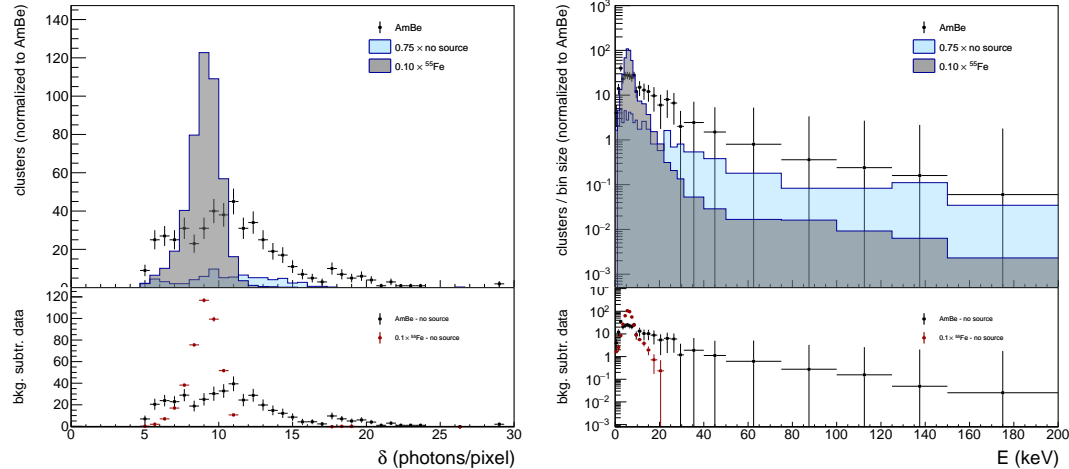


Figure 20. Supercluster light density δ (left) and calibrated energy E (right), after the preselection and cosmic ray suppression described in the text to select nuclear recoil candidates. Filled points represent data with AmBe source, dark gray (light blue) distribution represents data with ^{55}Fe source (no-source). The normalization of no-source data is to the same exposure time of the AmBe data, with the trigger scale factor ε_{SF} applied. For the data with ^{55}Fe , a scaling factor of one tenth is applied for clearness, given the larger activity of this source.

672 used to evaluate a curve of 5.9 keV electron recoils rejection $(1 - \varepsilon_B^\delta)$ as a function
 673 of signal efficiency (ε_S^δ), obtained varying the selection on δ , shown in Fig. 21. The
 674 same procedure could be applied to estimate the rejection factor against the cosmic ray
 675 induced background, but this is not shown because of the limited size of the no-source
 676 data. This kind of background will however be negligible when operating the detector
 677 underground, in the context of the CYGNO project, so no further estimates are given
 678 for this source.

679 Table 1 shows the full signal efficiency and electrons rejection factor for two example
 680 working points, WP₄₀ and WP₅₀, having 40% and 50% signal efficiency for the selection
 681 on δ , averaged over the full energy spectrum exploited in the AmBe data. They
 682 correspond to a selection $\delta > 11$ and $\delta > 10$, respectively. While this cut-based approach
 683 is minimalist, and could be improved by profiting of the correlations among δ and the
 684 observables used in the preselection in a more sophisticated multivariate analysis, it
 685 shows that a rejection factor approximately in the range $[10^{-3}-10^{-2}]$ of electron recoils
 686 at $E = 5.9$ keV with a gaseous detector at atmospheric pressure can be obtained, while
 687 retaining a high fraction of signal events.

688 6.4. Nuclear recoils energy spectrum and differential efficiency

689 The energy spectrum for the candidates with $\varepsilon_S^{total} = 50\%$ in the AmBe sample is shown
 690 in Fig. 22 (left). The signal efficiency is then computed for both the example working

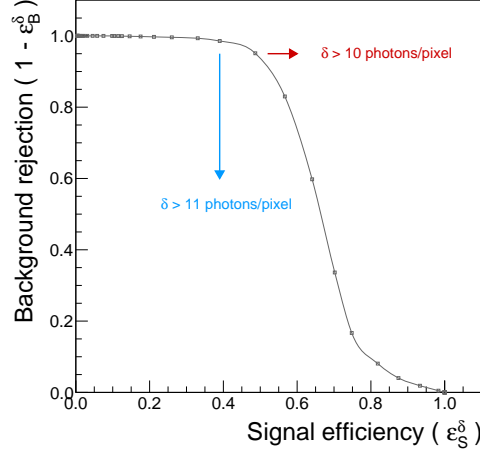


Figure 21. Background rejection as a function of the signal efficiency, varying the selection on the δ variable in data with either ^{55}Fe (background sample) or AmBe (signal sample) sources.

Table 1. Signal (nuclear recoils induced by AmBe radioactive source) and background (photo-electron recoils of X-rays with $E = 5.9\text{ keV}$ from ^{55}Fe radioactive source) efficiency for two different selections on δ .

working point	Signal efficiency			Background efficiency		
	$\varepsilon_S^{\text{presel}}$	ε_S^δ	$\varepsilon_S^{\text{total}}$	$\varepsilon_B^{\text{presel}}$	ε_B^δ	$\varepsilon_B^{\text{total}}$
WP ₅₀	0.98	0.51	0.50	0.70	0.050	0.035
WP ₄₀	0.98	0.41	0.40	0.70	0.012	0.008

points in bins of the visible energy. The efficiency, $\varepsilon_B^{\text{total}}$, represents a γ background efficiency at a fixed energy $E = 5.9\text{ keV}$, i.e., the energy of the photons emitted by the ^{55}Fe source. For the WP₅₀, the efficiency for very low-energy recoils, $E = 5.9\text{ keV}$, is still 18%, dropping to almost zero at $E \lesssim 4\text{ keV}$.

Two candidate nuclear recoils images, fulfilling the WP₅₀ selection (with a light density $\delta \gtrsim 10$ photons/pixels and with energies of 5.2 and 6.0 keV) are shown in Fig. 23. The displayed images are a portion of the full-resolution frame, after the pedestal subtraction. While the determination of the direction of detected nuclear recoil is still under study, it appears pretty clear from the image that some sensitivity to their direction, even at such low energies, is retained and can be further exploited.

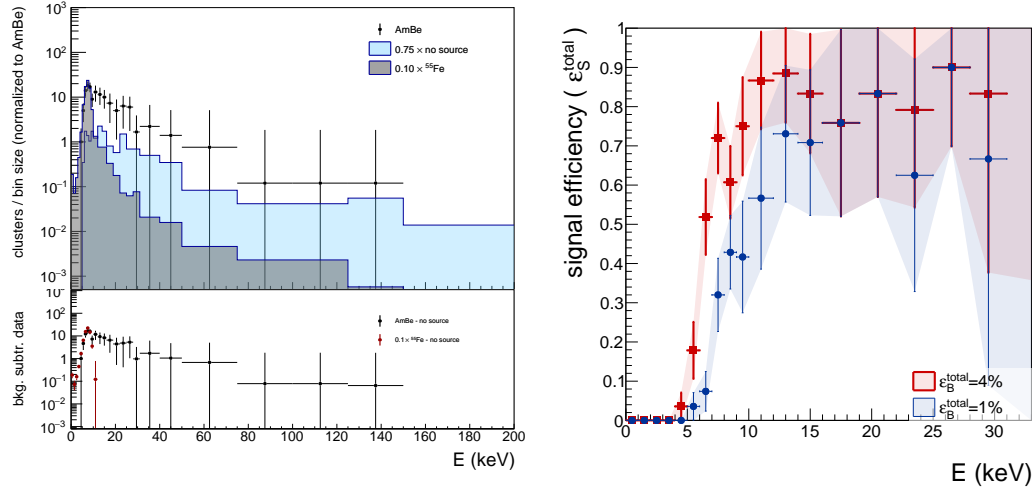


Figure 22. Left: supercluster calibrated energy E (left), after the full selection, which includes $\delta > 10$, 50% efficient on signal, to select nuclear recoil candidates. Filled points represent data with AmBe source, dark gray (light blue) distribution represents ^{55}Fe source (no-source) data. The normalization of no-source data is to the same exposure time of the AmBe data, with the trigger scale factor ϵ_{SF} applied. For the ^{55}Fe data, a scaling factor of one tenth is applied for clearness, given the larger activity of this source. Right: efficiency for nuclear recoil candidates as a function of energy, estimated on AmBe data, for two example selections, described in the text, having either 4% or 1% efficiency on electron recoils at $E = 5.9$ keV.

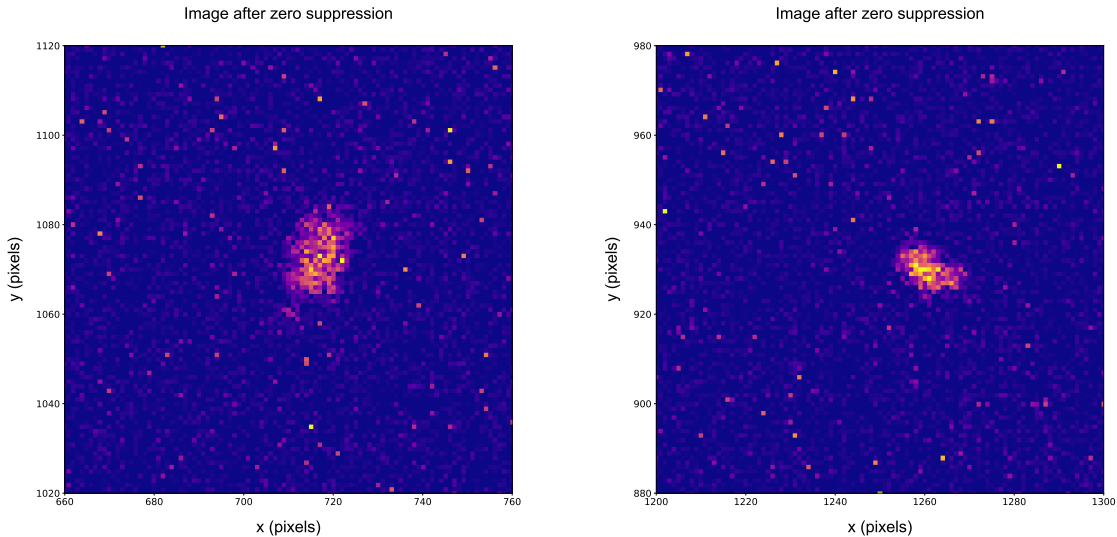


Figure 23. Examples of two nuclear recoil candidates, selected with the full selection, shown in a portion of 100×100 pixel matrix, after the zero suppression of the image. Left: a candidate with $E = 5.2$ keV and $\delta = 10.5$, right: a candidate with $E = 6.0$ keV and $\delta = 10$.

⁷⁰¹ **7. Conclusion and outlook**

⁷⁰² A method to efficiently identify recoiling nuclei after an elastic scattering with fast
⁷⁰³ neutrons with an optically readout TPC was presented in this paper. A 7 liter prototype
⁷⁰⁴ was employed by exposing its sensitive volume to two kinds of neutral particles in an
⁷⁰⁵ overground location:

- ⁷⁰⁶ • photons with energy of 5.9 keV and 59 keV respectively provided by a radioactive
⁷⁰⁷ source of ^{55}Fe and by one of ^{241}Am able to produce electron recoils with equal
⁷⁰⁸ energy by means of photoelectric effect;
- ⁷⁰⁹ • neutrons with kinetic energy of few MeV produced by an AmBe source that can
⁷¹⁰ create nuclear recoils with kinetic energy lower than the neutron ones.

⁷¹¹ The high sensitivity of the adopted sCMOS optical sensor allowed a very good
⁷¹² efficiency in detecting events with an energy released in gas even below 10 keV.

⁷¹³ Moreover, the possibility of exploiting the topological information (shape, size and
⁷¹⁴ more) of clusters of emitted light allowed to develop algorithms able to reconstruct not
⁷¹⁵ only the total deposited energy, but also to identify the kind of the recoiling ionizing
⁷¹⁶ particles in the gas (either an electron or a nucleus). Cosmic ray long tracks are also
⁷¹⁷ clearly separated.

⁷¹⁸ Because of their larger mass and electric charge, nuclear recoils are expected to
⁷¹⁹ release their energy by ionizing the gas molecules in few hundreds μm while the electrons
⁷²⁰ are able to travel longer paths. For this reason, by exploiting the spatial distribution of
⁷²¹ the collected light, it was possible to identify 5.9 keV electron recoils with an efficiency
⁷²² of 96.5% (99.2%) against nuclear recoils by retaining a capability of detecting them with
⁷²³ an efficiency of 50% (40%), averaged across the measured AmBe spectrum.

⁷²⁴ In particular, the nuclear recoil detection efficiency was measured to be 40% for
⁷²⁵ deposited energies lower than 20 keV and 14% in the range (5–10) keV.

⁷²⁶ The results obtained in the studies presented in this paper can be improved
⁷²⁷ by means of more sophisticated analyses exploiting a multivariate approach, which
⁷²⁸ combines a more complete topological information about the light distribution along
⁷²⁹ the tracks. Additional enhancement of sensitivity can be achieved with a DAQ system
⁷³⁰ collecting single PMT waveforms to be correlated with the track reconstructed in the
⁷³¹ sCMOS images.

⁷³² **8. Acknowledgements**

⁷³³ We are grateful to Servizio Sorgente LNF... This work was supported by the European
⁷³⁴ Research Council (ERC) under the European Union's Horizon 2020 research and
⁷³⁵ innovation program (grant agreement No 818744)".

⁷³⁶ [1] B. W. Lee and S. Weinberg, "Cosmological lower bound on heavy-neutrino masses," *Phys. Rev. Lett.*, vol. 39, pp. 165–168, Jul 1977.

⁷³⁸ [2] T. M. Undagoitia and L. Rauch, "Dark matter direct-detection experiments," *Journal of Physics G: Nuclear and Particle Physics*, vol. 43, p. 013001, dec 2015.

- [3] Y. Hochberg, E. Kuflik, T. Volansky, and J. G. Wacker, “Mechanism for thermal relic dark matter of strongly interacting massive particles,” *Phys. Rev. Lett.*, vol. 113, p. 171301, Oct 2014.
- [4] D. E. Kaplan, M. A. Luty, and K. M. Zurek, “Asymmetric dark matter,” *Phys. Rev. D*, vol. 79, p. 115016, Jun 2009.
- [5] K. PETRAKI and R. R. VOLKAS, “Review of asymmetric dark matter,” *International Journal of Modern Physics A*, vol. 28, no. 19, p. 1330028, 2013.
- [6] K. M. Zurek, “Asymmetric dark matter: Theories, signatures, and constraints,” *Physics Reports*, vol. 537, no. 3, pp. 91 – 121, 2014. Asymmetric Dark Matter: Theories, signatures, and constraints.
- [7] F. Mayet, A. Green, J. Battat, J. Billard, N. Bozorgnia, G. Gelmini, P. Gondolo, B. Kavanagh, S. Lee, D. Loomba, J. Monroe, B. Morgan, C. O’Hare, A. Peter, N. Phan, and S. Vahsen, “A review of the discovery reach of directional dark matter detection,” *Physics Reports*, vol. 627, pp. 1 – 49, 2016. A review of the discovery reach of directional Dark Matter detection.
- [8] E. Baracchini, G. Cavoto, G. Mazzitelli, F. Murtas, F. Renga, and S. Tomassini, “Negative ion time projection chamber operation with SF₆ at nearly atmospheric pressure,” *Journal of Instrumentation*, vol. 13, pp. P04022–P04022, Apr. 2018.
- [9] M. Marafini, V. Patera, D. Pinci, A. Sarti, A. Sciubba, and E. Spiriti, “ORANGE: A high sensitivity particle tracker based on optically read out GEM,” *Nucl. Instrum. Meth.*, vol. A845, pp. 285–288, 2017.
- [10] V. C. Antochi, E. Baracchini, G. Cavoto, E. D. Marco, M. Marafini, G. Mazzitelli, D. Pinci, F. Renga, S. Tomassini, and C. Voena, “Combined readout of a triple-GEM detector,” *JINST*, vol. 13, no. 05, p. P05001, 2018.
- [11] D. Pinci, E. Di Marco, F. Renga, C. Voena, E. Baracchini, G. Mazzitelli, A. Tomassini, G. Cavoto, V. C. Antochi, and M. Marafini, “Cygnus: development of a high resolution TPC for rare events,” *PoS*, vol. EPS-HEP2017, p. 077, 2017.
- [12] G. Mazzitelli, V. A. Antochi, E. Baracchini, G. Cavoto, A. De Stena, E. Di Marco, M. Marafini, D. Pinci, F. Renga, S. Tomassini, and C. Voena, “A high resolution TPC based on GEM optical readout,” in *2017 IEEE Nuclear Science Symposium and Medical Imaging Conference (NSS/MIC)*, pp. 1–4, Oct 2017.
- [13] D. Pinci, E. Baracchini, G. Cavoto, E. Di Marco, M. Marafini, G. Mazzitelli, F. Renga, S. Tomassini, and C. Voena, “High resolution TPC based on optically readout GEM,” *Nuclear Instruments and Methods in Physics Research Section A: Accelerators, Spectrometers, Detectors and Associated Equipment*, 2018.
- [14] I. A. Costa, E. Baracchini, R. Bedogni, F. Bellini, L. Benussi, S. Bianco, M. Caponero, G. Cavoto, E. D. Marco, G. D’Imperio, G. Maccarrone, M. Marafini, G. Mazzitelli, A. Messina, F. Petrucci, D. Piccolo, D. Pinci, F. Renga, G. Saviano, and S. Tomassini, “CYGNO: Triple-GEM optical readout for directional dark matter search,” *Journal of Physics: Conference Series*, vol. 1498, p. 012016, apr 2020.
- [15] C. Collaboration, “CYGNO Phase-I: One cubic meter demonstrator.” <https://web.infn.it/cygnus/cygno>, 2020.
- [16] D. Pinci, *A triple-GEM detector for the muon system of the LHCb experiment*. PhD thesis, Cagliari University, CERN-THESIS-2006-070, 2006.
- [17] Hamamatsu, *ORCA-Flash4.0 V3 Digital CMOS camera*, 2018. <http://www.hamamatsu.com/jp/en/C13440-20CU.html>.
- [18] M. Marafini, V. Patera, D. Pinci, A. Sarti, A. Sciubba, and E. Spiriti, “High granularity tracker based on a Triple-GEM optically read by a CMOS-based camera,” *JINST*, vol. 10, no. 12, p. P12010, 2015.
- [19] HZC Photonics, *XP3392 Photomultiplier*. <http://www.hzcphotonics.com/products/XP3392.pdf>.
- [20] V. C. Antochi, G. Cavoto, I. Abritta Corsta, E. Di Marco, G. D’Imperio, F. Iacoangeli, M. Marafini, A. Messina, D. Pinci, F. Renga, C. Voena, E. Baracchini, A. Cortez, G. Dho, L. Benussi,

- 791 S. Bianco, C. Capoccia, M. Caponero, G. Maccarrone, G. Mazzitelli, A. Orlandi, E. Paoletti,
 792 L. Passamonti, D. Piccolo, D. Pierluigi, F. Rosatelli, A. Russo, G. Saviano, S. Tomassini, R. A.
 793 Nobrega, and F. Petrucci, “A GEM-based optically readout time projection chamber for charged
 794 particle tracking,” 2020.
- 795 [21] R. Campagnola, “Study and optimization of the light-yield of a triple-GEM detector ,” Master’s
 796 thesis, Sapienza University of Rome, 2018.
- 797 [22] N. Torchia, “Development of a tracker based on GEM optically readout ,” Master’s thesis, Sapienza
 798 University of Rome, 2016.
- 799 [23] CAEN, *2 Channel 15 kV/1 mA (10 W) NIM HV Power Supply Module*, 2017. <http://www.caen.it/csite/CaenProd.jsp?parent=21&idmod=894>.
- 800 [24] R. Veenhof, “GARFIELD, recent developments,” *Nucl. Instrum. Meth. A*, vol. 419, pp. 726–730,
 801 1998.
- 802 [25] R. Veenhof, “GARFIELD, a drift chamber simulation program,” *Conf. Proc. C*, vol. 9306149,
 803 pp. 66–71, 1993.
- 804 [26] G. Mazzitelli, A. Ghigo, F. Sannibale, P. Valente, and G. Vignola, “Commissioning of the
 805 DA ϕ NE beam test facility,” *Nuclear Instruments and Methods in Physics Research Section A: Accelerators, Spectrometers, Detectors and Associated Equipment*, vol. 515, no. 3, pp. 524 – 542,
 806 2003.
- 807 [27] I. Abritta Costa, E. Baracchini, F. Bellini, L. Benussi, S. Bianco, M. A. Caponero, G. Cavoto,
 808 G. D’Imperio, E. Di Marco, G. Maccarrone, M. Marafini, G. Mazzitelli, A. Messina, F. Petrucci,
 809 D. Piccolo, D. Pinci, F. Renga, F. Rosatelli, G. Saviano, and S. Tomassini, “Stability and
 810 detection performance of a GEM-based optical readout TPC with He/CF₄ gas mixtures,” *Journal of Instrumentation*, vol. xx, p. xxx, jul 2020.
- 811 [28] S. Agostinelli *et al.*, “GEANT4—a simulation toolkit,” *Nucl. Instrum. Meth. A*, vol. 506, p. 250,
 812 2003.
- 813 [29] J. Ziegler, “Srim – 2003,” *Nuclear Instruments and Methods in Physics Research Section B: Beam Interactions with Materials and Atoms*, vol. 219-220, no. 3, pp. 1027–1036, 2004.
- 814 [30] I. Abritta Costa, E. Baracchini, F. Bellini, L. Benussi, S. Bianco, M. A. Caponero, G. Cavoto,
 815 G. D’Imperio, E. Di Marco, G. Maccarrone, M. Marafini, G. Mazzitelli, A. Messina, F. Petrucci,
 816 D. Piccolo, D. Pinci, F. Renga, F. Rosatelli, G. Saviano, and S. Tomassini, “Performance of
 817 optically readout GEM-based TPC with a ⁵⁵Fe source,” *Journal of Instrumentation*, vol. 14,
 818 pp. P07011–P07011, jul 2019.
- 819 [31] Y. Dong and S. Xu, “A new directional weighted median filter for removal of random-valued impulse
 820 noise,” *IEEE Signal Processing Letters*, vol. 14, no. 3, pp. 193–196, 2007.
- 821 [32] G. S. P. Lopes, E. Baracchini, F. Bellini, L. Benussi, S. Bianco, G. Cavoto, I. A. Costa, E. Di Marco,
 822 G. Maccarrone, M. Marafini, G. Mazzitelli, A. Messina, R. A. Nobrega, D. Piccolo, D. Pinci,
 823 F. Renga, F. Rosatelli, D. M. Souza, and S. Tomassini, “Study of the impact of pre-processing
 824 applied to images acquired by the cygno experiment,” in *Pattern Recognition and Image Analysis*
 825 (A. Morales, J. Fierrez, J. S. Sánchez, and B. Ribeiro, eds.), (Cham), pp. 520–530, Springer
 826 International Publishing, 2019.
- 827 [33] I. Abritta *et al.*, “A density-based clustering algorithm for the cygno data analysis,” *In preparation*,
 828 vol. 00, no. 0, pp. 00–00, 2020.
- 829 [34] M. Ester, H.-P. Kriegel, J. Sander, and X. Xu, “A density-based algorithm for discovering clusters
 830 in large spatial databases with noise,” pp. 226–231, AAAI Press, 1996.
- 831 [35] G. Van Rossum and F. L. Drake, *Python 3 Reference Manual*. Scotts Valley, CA: CreateSpace,
 832 2009.
- 833 [36] R. Brun and F. Rademakers, “ROOT: An object oriented data analysis framework,” *Nucl. Instrum. Meth. A*, vol. 389, pp. 81–86, 1997.
- 834 [37] V. Caselles, R. Kimmel, and G. Sapiro, “Geodesic Active Contours,” *International Journal of Computer Vision*, vol. 22, pp. 61–79, 1997.
- 835 [38] P. Márquez-Neila, L. Baumela, and L. Alvarez, “A morphological approach to curvature-based

842 evolution of curves and surfaces," *IEEE Transactions on Pattern Analysis and Machine*
843 *Intelligence*, vol. 36, no. 1, pp. 2–17, 2014.

844 [39] Z. Guo and R. W. Hall, "Parallel thinning with two-subiteration algorithms," *Commun. ACM*,
845 vol. 32, p. 359–373, Mar 1989.

846 [40] L. Lam, S. Lee, and C. Y. Suen, "Thinning methodologies - a comprehensive survey," *IEEE*
847 *Transactions on Pattern Analysis and Machine Intelligence*, vol. 14, no. 9, pp. 869–885, 1992.